Corrosion Science 228 (2024) 111831

Contents lists available at ScienceDirect

Corrosion Science

journal homepage: www.elsevier.com/locate/corsci

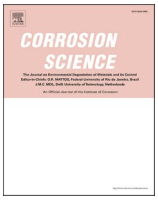

An investigation of the long-term aqueous corrosion behaviour of glass-zirconolite composite materials (Fe-Al-BG-$CaZrTi_2O_7$) as a potential nuclear wasteform

Mehrnaz Mikhchian, Andrew P. Grosvenor *

Department of Chemistry, University of Saskatchewan, Saskatoon, Saskatchewan S7N5C9, Canada

ARTICLE INFO

Keywords:
Nuclear wasteform
Zirconolite
Corrosion resistance
Surface chemistry
Leaching rates

ABSTRACT

The long-term aqueous corrosion behaviour of Fe-Al borosilicate glass-zirconolite (Fe-Al-BG-$CaZrTi_2O_7$) glass-ceramic composite materials results from incongruent and congruent corrosion mechanisms of the individual zirconolite ($CaZrTi_2O_7$) and Fe-Al borosilicate glass (Fe-Al-BG) phases after the Fe-Al-BG-$CaZrTi_2O_7$ composite materials were exposed to deionised water for 365 days. A comprehensive investigation of the aqueous corrosion resistance and structural stability of Fe-Al-BG-$CaZrTi_2O_7$ composite materials has demonstrated that the proposed glass-ceramic composite materials are chemically durable over long-term exposure to water and can be considered as potential alternative hosts to borosilicate glass for the safe and effective disposal of nuclear waste.

1. Introduction

Nuclear power is considered a clean alternative source of electricity compared to fossil fuels; however, safe disposal of high-level radioactive waste (spent nuclear fuel) remains a key problem for the sustainable development of the nuclear industry. Geological disposal is a proposed method for the permanent disposal of high-level radioactive waste (HLW) in many countries [1–3]. Generally, geological sequestration involves the immobilisation of the nuclear waste elements into a wasteform, storing the wasteform in a container, and placing the container in a deep geological repository. A common challenge associated with geological disposal is groundwater corrosion and leaching of the radionuclides incorporated in a wasteform into the environment [1–4]. Therefore, materials proposed for the immobilisation of radioactive elements known as "wasteforms" must have high chemical durability and be thermodynamically stable under the temperature and pressure conditions of the repository over long periods [1–4].

Nuclear wasteforms can be classified as glass, ceramic, and glass-ceramic composite materials, which can incorporate radioactive elements into either amorphous or crystalline phases [1,2,4]. Glass wasteforms are the first-generation nuclear wasteform that is used in many countries as a potential wasteform for the immobilisation of HLW [5,6]. Numerous studies have been carried out to understand the long-term leaching behaviour of glass materials in aqueous solutions due to their capacity to accommodate a large variety of small radionuclides (i.e., compared to large actinide waste elements) and fission products into the amorphous structure [5,6]. Despite the applications of silicate glasses as a wasteform, these amorphous wasteforms have several disadvantages, such as lower thermal stability and chemical durability, lower loading limit of actinide elements, and higher dissolution rates over geological timescales upon exposure to aqueous environments compared to ceramics and glass-ceramic composite wasteforms [7–10]. To overcome these issues, crystalline ceramic materials have been proposed as an alternative wasteform because of their higher chemical durability compared to glass wasteforms [11,12]. However, ceramic materials are limited in the variety of waste elements that can be incorporated into the specific crystallographic sites of ceramics based on the size, bond length, and oxidation state of the ions [11,12]. Due to the increasing demand for the immobilisation of large quantities of high-level nuclear waste, glass-ceramic composite materials have been developed as a new candidate wasteform for nuclear waste sequestration [7,13].

Glass-ceramic composite materials consist of single or multi-phase crystalline materials dispersed in an amorphous glass matrix [12,14,15]. The vitrification process is a current method for the immobilisation of the HLW stream into the glass wasteform that is based on melt and quench techniques [6,8]. Several studies on glass-ceramic wasteforms have shown that these materials can be processed using the current

* Corresponding author.
E-mail address: andrew.grosvenor@usask.ca (A.P. Grosvenor).

https://doi.org/10.1016/j.corsci.2024.111831
Received 6 September 2023; Received in revised form 19 December 2023; Accepted 3 January 2024
Available online 6 January 2024
0010-938X/© 2024 The Authors. Published by Elsevier Ltd. This is an open access article under the CC BY-NC-ND license (http://creativecommons.org/licenses/by-nc-nd/4.0/).

method that is used for the glass wasteform (melting and quenching), in which metal oxide precursors of crystalline ceramic and glass are mixed and annealed to form a glass-ceramic composite [12,14]. The glass matrix can incorporate a wide range of small radionuclides (i.e., compared to large actinide waste elements) and fission products, while the ceramic phase can incorporate actinides (and other larger waste elements) into specific crystallographic sites in the crystalline structure (s) [2,3]. Various types of glasses have been used for the synthesis of glass-ceramic composites; however, borosilicate glass (BG) and Fe-Al borosilicate glass (Fe-Al-BG) are the most widely used glasses because of the stability and flexibility of the silicate network [5,16]. The presence of transition metals (e.g., Fe) in borosilicate glass can enhance the radiation resistance of these wasteforms through trapping electron-hole pairs caused by nuclear radiation [12,16,17]. Moreover, using alumina (Al_2O_3) in borosilicate glass can prevent the formation of crystalline SiO_2, which can cause cracks in the glass wasteform at low temperatures and eventually decrease the leaching resistance of the silicate network [12,16,17]. In glass-ceramic composite materials, the glass matrix can act as a secondary barrier to the crystallites and enhance the chemical durability of the composite materials in contact with an aqueous solution [14,18]. However, most studies on the aqueous corrosion of glass-ceramic composite materials are limited to short-term leaching experiments (e.g., 14–56 days), which might not be adequate to evaluate their chemical durability and dissolution behaviours [7,10,13,14,18]. The focus of this study was to investigate the differences and similarities of the long-term corrosion behaviour of Fe-Al-BG-$CaZrTi_2O_7$ composite materials compared to Fe-Al-BG and $CaZrTi_2O_7$ in deionised water as a preliminary step to determine if Fe-Al-BG-$CaZrTi_2O_7$ composite materials should be further considered as a potential nuclear wasteform. The crystalline ceramic zirconolite oxide phase has been proposed for this application due to its high chemical durability and ability to substitute actinides and lanthanide elements of up to 25 wt% in the structure [2,3,19–21]. The 2M-polytype of zirconolite has a monoclinic crystal structure with the space group C2/c, and the general formula of $CaZrTi_2O_7$. The zirconolite structure consists of two different cation layers, one composed of 8-coordinate Ca^{2+} and 7-coordinate Zr^{4+}, and the other of corner-sharing 5- and 6-coordinate Ti^{4+} (Fig. 1) [15,22,23]. Actinide and lanthanide elements can be incorporated into Zr^{4+} or Ca^{2+} sites of the zirconolite crystal structure based on their size, bond length, and oxidation state [20,21].

The long-term leaching behaviour of wasteform materials depends on the structure and composition of the materials, leaching duration, temperature, composition, and pH of the leachant solution [3–6,14]. Several standard test protocols have been proposed in order to investigate the leaching mechanism of wasteform materials for nuclear waste disposal applications [25–27]. These tests provide comprehensive information that can be used to assess the performance of wasteform materials and address possible challenges that might happen in geological disposal facilities. Among them, the widely used standard protocols include the product consistency tests (PCT), a series of chemical durability tests by the materials characterisation centre (MCC-1 – MCC-5), the vapour hydration test (VHT), and single-pass flow-through tests (SPFT) [25,27–29]. Selecting the leaching method to use depends on the leaching condition (static or dynamic), the type of the wasteform material (i.e., monolithic or powdered material), and structure (amorphous vs. crystalline) [25–29]. The PCT-B (ASTM C1285) test has been selected in this study, which is one of the standard durability tests that can be conducted on powdered/crushed materials under varied leaching conditions (i.e., different test durations, surface area to volume ratios (SA/V), temperatures, and leachant volume, and composition) to determine the long-term leaching mechanism of the proposed wasteform materials [26–28,30–36] This test is a static test and the wasteform is ground to increase the surface area exposed to the leachant solution [26,27]. Under static conditions, the wasteforms are in contact with a constant volume of leachant solution, and the concentration of leached ions released into the leachant is determined over the test duration [11,27,32–34]. Therefore, the leaching rates initially increase with time as the wasteform components release into the leachant. Once the leachant solution reaches saturation and the ions reached the solubility limit, the leaching rates will decrease or remain constant [11,26–28,30,32]. In this study, the leachate solutions were analysed regularly by inductively coupled plasma-mass spectrometry (ICP-MS) over a period of 365 days to determine the concentration of ions leached from the Fe-Al-BG, $CaZrTi_2O_7$, and Fe-Al-BG-$CaZrTi_2O_7$ composite materials. The phase composition, local chemical environment, and bulk and surface chemical environments of the materials were studied using powder X-ray diffraction (XRD) and X-ray absorption near-edge spectroscopy (XANES) before, during, and after leaching to investigate the corrosion resistance of these materials as potential candidate wasteforms over a long period. The data obtained from the long-term leaching studies of the Fe-Al-BG, $CaZrTi_2O_7$, and Fe-Al-BG-$CaZrTi_2O_7$ composite materials provide important information on the corrosion mechanisms and performance of the Fe-Al-BG-$CaZrTi_2O_7$ composite as a potential host for the immobilisation of high-level and intermediate level nuclear waste in future geological repositories.

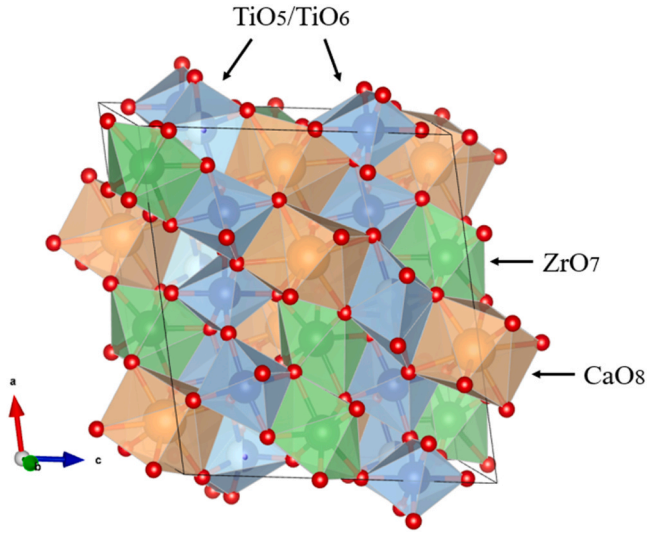

Fig. 1. 2 M polytype zirconolite structure showing 8-coordinate Ca, 7-coordinate Zr, and corner-sharing 6-coordinate and 5-coordinate Ti [15,22,23]. The crystal structures were generated using the VESTA software programme [24].

2. Materials and methods

2.1. Synthesis of wasteform materials

2.1.1. Synthesis of Fe-Al borosilicate glasses

Fe-Al borosilicate glass (Fe-Al-BG) was made using the conventional ceramic method. The mole and weight percentages of the binary compounds used for the synthesis of a 0.25 g of Fe-Al-BG were 55.5 mol% (49.8 wt%) SiO_2 (EMD Millipore), 16.9 mol% (17.6 wt%) B_2O_3 (Alfa Aesar; 99.98%), 16.5 mol% (15.3 wt%) Na_2O (Alfa Aesar), 3.1 mol% (2.6 wt%) CaO (Acros Organics; 97 +%), 5.0 mol% (7.6 wt%) Al_2O_3 (Sigma-Aldrich; 98%), and 3.0 mol% (7.1 wt%) Fe_2O_3 (Alfa Aesar; 99.945%). The oxide powders were mixed, ground, and pressed into a pellet at 6 MPa and annealed in 5% Au/ 95% Pt crucibles at 1100 °C for 1 h, followed by quench cooling in water. The Fe-Al-BG sample was quenched cooled in water to limit crystallisation.

2.1.2. Synthesis of zirconolite-type oxides

Zirconolite ($CaZrTi_2O_7$) was synthesised by the ceramic method using stoichiometric amounts of $CaCO_3$ (EMD, ≥99.0%), ZrO_2 (Alfa Aesar, 99.7%), and TiO_2 (Alfa Aesar, anatase, 99.6%) powders with a molar ratio of 1:1:2. The mole and weight percentages of binary oxides

were 24.8 mol% (29.5 wt%) $CaCO_3$, 24.8 mol% (36.3 wt%) ZrO_2, and 50.4 mol% (47.1 wt%) TiO_2. The oxide powders were ground, pressed into pellets at 6 MPa, and heated in air at 1400 °C for three days in an alumina crucible followed by quench cooling in air to room temperature. After three days of annealing, the samples were ground, pelleted, and re-heated at 1400 °C for three more days to obtain a phase pure material and quench cooled in air.

2.1.3. Synthesis of glass-zirconolite composite materials

The Fe-Al-BG-$CaZrTi_2O_7$ composite materials containing 40 wt% of $CaZrTi_2O_7$ crystallites dispersed in 60 wt% of Fe-Al-BG were synthesised using a 2-step ceramic method. The separately synthesised Fe-Al-BG and $CaZrTi_2O_7$ materials were mixed, ground, pressed into pellets at 6 MPa, and then annealed in 5% Au/95% Pt crucibles at 750 °C for 1 h to form the glass-ceramic composite material. The Fe-Al-BG-$CaZrTi_2O_7$ composite materials were quench cooled in water to room temperature to maintain the amorphous structure of the Fe-Al-BG matrix. The phase analysis of as-synthesised $CaZrTi_2O_7$ and Fe-Al-BG-$CaZrTi_2O_7$ composite materials, as determined by powder XRD, is shown in Fig. S1.

2.2. BET analysis

The materials were finely ground before determining the surface areas. The materials were degassed at ~120 °C and the specific surface areas ($SA_{specific}$) were determined by nitrogen adsorption measurements using a Brunauer-Emmett-Teller (BET) instrument (Micromeritics ASAP 2020 (Norcross, GA)) before starting the leaching experiments [37]. The results of this analysis are reported in Table 1.

2.3. Leaching experiments

The PCT-B (ASTM C1285) standard leaching test has been used in this study with slight modifications to measure the chemical durability of proposed Fe-Al-BG, $CaZrTi_2O_7$, and Fe-Al-BG-$CaZrTi_2O_7$ composite materials under either static or semi-static condition [26–28]. Based on the PCT-B standard method, the volume of leachant is approximately 10 times the sample mass [26–28]. However, the volume of leachant used in this work was higher to make sure that the powders were completely immersed in the deionised water. Deionised water has been used in this study as it is considered a standard leachant solution in various leaching tests for evaluation of the chemical durability of wasteform materials [26,27]. It should be noted that the composition of groundwater is different from the deionised water and could change depending on the location of deep geological repositories [26,27]. The as-synthesised Fe-Al-BG, $CaZrTi_2O_7$, and Fe-Al-BG-$CaZrTi_2O_7$ composite materials were finely ground before performing the aqueous corrosion study to increase the surface area of the samples exposed to water. Increasing the surface area (SA_{total}) of the material to the volume of the leachant solution is one of the common methods to accelerate the dissolution of wasteforms, which can provide useful information to assess the behaviour of the wasteforms over geological time [3,36]. The ratio of the total surface area (SA_{total}) of the material to the volume of the leachant solution (V) was 30 cm^{-1}. Generally, for the powdered material, especially using wasteforms with low leach rates, the higher range of SA_{total}/V values is used to measure the low concentration of the leached elements in the leachate [7,13,27,28]. It has been reported in the literature that using high SA_{total}/V values could result in lower leaching rates with time and forming a thinner alteration layer [11,27,28,30,35]. The total surface area (SA_{total}) was obtained by multiplying the $SA_{specific}$ of each material by the mass of the material. The as-synthesised Fe-Al-BG, $CaZrTi_2O_7$, and Fe-Al-BG-$CaZrTi_2O_7$ composite materials were sieved and the particle size varied from 45–110 μm. Individual samples of the Fe-Al-BG, $CaZrTi_2O_7$, and Fe-Al-BG-$CaZrTi_2O_7$ composite materials were placed inside high-density polyethylene (HDPE) containers and were filled with different volumes of deionised water (based on the mass of the samples) as the leachant solution. The specific surface areas ($SA_{specific}$) and average particle sizes determined using BET analysis, and the calculated total surface area (SA_{total}), the volume of water, and the required mass of the materials for the leaching experiments are listed in Table 1. The leaching tests were carried out at room temperature using deionised water at near neutral pH (i.e., ~ 7) under either static or semi-static conditions over 365 days.

In the static experiments, the materials were exposed to a constant volume of deionised water over the entire leaching period without withdrawing the leachant solution from the containers. Each container was stirred manually once every day to accelerate leaching and the solid materials were collected and dried after 30, 90, 180, 270, and 365 days of exposure to the leachant solution.

The semi-static leaching experiments were performed in triplicate on each material (i.e., Fe-Al-BG, $CaZrTi_2O_7$, and Fe-Al-BG-$CaZrTi_2O_7$ composite). The semi-static experiments involved withdrawing and then replacing 5 mL aliquots of the leachate solution at set time intervals of 0, 1, 3, 5, 8, 15, 30, 60, 90 days and then every 60 days up to 365 days. These tests can represent the slow flow rate of groundwater in contact with wasteform in geological repositories [26]. Each container was stirred manually once every day to accelerate the leaching process and the leachate solution was left undisturbed for 24 h to allow the solids to settle before collecting the leachate solution for ICP-MS analysis. The leachates were collected from near the top of the container to avoid collecting solid materials. It should be noted that no visible particles were observed in the leachate solutions prior to the ICP-MS analysis. The collected leachate solutions were regularly analysed using ICP-MS (Agilent 8900 Triple Quadrupole) located at the Fipke Laboratory for Trace Element Research (FiLTER), University of British Columbia - Okanagan. To study the corrosion behaviour of Fe-Al-BG in deionised water, the collected leachates were analysed to determine the concentration of B, Na, Fe, Al, and Ca ions in the leachate solution. In the case of the dissolution behaviour of $CaZrTi_2O_7$, the concentration of Ca, Zr, and Ti ions was measured in the leachate solutions. Moreover, the collected leachates in contact with the Fe-Al-BG-$CaZrTi_2O_7$ composite materials were analysed for the presence of B, Na, Fe, Al, Ca, Zr, and Ti ions.

ICP-MS data was collected frequently from a blank solution (deionised water) to determine the concentration of ions in the deionised water used for this study, and the data is available in the supplementary material (Table S1). The instrumental limit of detection (LOD) ranges for the ions in leachate were: 0.25–3.21 ppb (Na), 0.01–5.05 ppb (Ca), 0.01–2.04 ppb (B), 3.12–577.59 ppb (Si), 0.01–1.09 ppb (Fe), 0.01–2.38 ppb (Al), 0.01–0.03 ppb (Zr), and 0.01–0.11 ppb (Ti). The ICP-MS instrument used in this study contained silicate glass components which can influence the reliability of the detected Si signal from the leachate. As such, the concentrations of Si in the leachate determined by ICP-MS from the Fe-Al-BG and Fe-Al-BG-$CaZrTi_2O_7$ composite samples are not considered to be reliable and are only used as a reference (Fig. S2).

The normalised mass loss (N_L; g m^{-2}) and the normalised leach rate

Table 1
Measured specific surface area and particle size using BET, and calculated total surface area, mass of wasteform materials, and required volume of water for the leaching experiments.

Compound	Specific surface area (m^2/g)	Average particle size (nm)	Total surface area (m^2)	Mass of a material (g)	Volume of water required (L)
$CaZrTi_2O_7$	1.23	4878	0.3075	0.2500	0.1025
Fe-Al-BG	1.87	3216	0.3366	0.1800	0.1120
Fe-Al-BG-$CaZrTi_2O_7$	1.55	3876	0.3255	0.2100	0.1085

(R_L; g $m^{-2}d^{-1}$) of ions were calculated at regular intervals using the following equations [7,33,38,39].

$$N_L = \frac{C \times V}{f \times SA_{Total}} \quad (1)$$

$$R_L = \frac{C \times V}{f \times SA_{Total} \times t} \quad (2)$$

In these equations, C indicates the concentration of the leached ion in the leachate (g/L), V is the volume of the leachant (L), f is the mass fraction of the leached ion in the solid, SA_{Total} is the total surface area of the solid (m^2), and t is the duration of the experiment in days.

The concentration, normalised mass loss, and the normalised leach rate of ions were reported by calculating the average and standard deviation of dissolved ions from each material (i.e., Fe-Al-BG, $CaZrTi_2O_7$, and Fe-Al-BG-$CaZrTi_2O_7$ composite) at above mentioned set time intervals based on performing triplicate semi-static leaching experiments.

2.4. Powder X-ray diffraction

Powder X-ray diffraction patterns from the Fe-Al-BG, $CaZrTi_2O_7$, and Fe-Al-BG-$CaZrTi_2O_7$ composite materials before, during, and after completion of the static leaching experiments were collected using a Rigaku Ultima IV X-Ray Diffractometer with a Cu $K\alpha_{1,2}$ X-ray source operating at 40 kV and 44 mA. Diffraction patterns were scanned in the 2θ range from 10° to 80° with a step size of 0.02° and a scan rate of 3° per minute for phase analysis. The phase analysis was performed using the PowderCell for Windows software programme [40]. The measured powder patterns were compared with the calculated XRD patterns from the Inorganic Crystal Structure Database (ICSD) [41].

2.5. X-ray absorption near-edge spectroscopy (XANES)

X-ray absorption spectroscopy (XAS) is an element-specific technique that provides information on the electronic structure and local chemical environment (i.e., oxidation state and coordination environment) of elements within materials [11,12]. The principle of this technique is based on an excitation of a core electron of the element of interest with a specific energy into unoccupied conduction states above the Fermi level [11,12,16]. XAS can be used to study a wide variety of materials that can be either crystalline or amorphous [11,12]. A typical XAS spectrum consists of two regions: the X-ray absorption near edge spectroscopy (XANES) region and the extended X-ray absorption fine structure (EXAFS) region. XANES spectra include a main-edge feature resulting from a dipolar transition ($\Delta l = \pm 1$), which starts from 5 eV below the absorption edge and usually covers up to 50 eV above the absorption edge [11,12]. Moreover, in the XANES spectra of transition metals a low-energy pre-edge feature appears that results from a quadrupolar transition ($\Delta l = \pm 2$) which is sensitive to changes in coordination number [11,12,16]. Depending on the density of materials, X-ray photon energy, and attenuation length, the XANES spectra can provide information at different sampling depths [16]. XANES spectra collected using high-energy X-rays (i.e., hard X-rays) in transmission or fluorescence modes are bulk sensitive, whereas the XANES spectra collected using low-energy X-rays (i.e., soft X-rays) in fluorescence mode are surface sensitive [11,12,16]. A combination of hard and soft X-ray XANES measurements have been used in this study to understand how the surface and bulk regions of materials change as a result of corrosion.

2.5.1. Ti, Zr and Fe K-edge XANES

The Ti, Zr, and Fe K-edge XANES spectra were collected using the Sector 9 bending magnet (9BM) beamline located at the Advanced Photon Source (APS), Argonne National Laboratory [42]. Samples were prepared by spreading finely ground powders on Kapton tape and folding the tape to produce multiple layers. The energy of the XANES spectra was increased by 0.15 eV per step through the absorption edge for the Ti and Fe K-edge spectra, and 0.3 eV per step through the absorption edge for the Zr K-edge spectra. The Ti, Zr, and Fe K-edge XANES spectra were calibrated by setting the maximum of the first derivative of a spectrum from Ti foil to 4966 eV, Zr foil to 17,998 eV, and Fe foil to 7112 eV [43,44]. Ti K-edge XANES spectra from the bulk of $CaZrTi_2O_7$ and Fe-Al-BG-$CaZrTi_2O_7$ composite materials were collected in transmission mode with the attenuation length of photons of ~ 6 μm and ~ 9 μm, respectively. Zr K-edge XANES spectra from the bulk of $CaZrTi_2O_7$ and Fe-Al-BG-$CaZrTi_2O_7$ composite materials were collected in transmission mode with the attenuation length of photons of ~ 42 μm and ~ 66 μm, respectively. Fe K-edge XANES spectra from the bulk of Fe-Al-BG and Fe-Al-BG-$CaZrTi_2O_7$ composite materials were collected in transmission mode with the attenuation length of photons of ~ 29 μm and ~ 17 μm, respectively. The attenuation length of photons for the Ti, Zr, and Fe having the above energies was calculated using the approximate density of $CaZrTi_2O_7$, Fe-Al-BG, and Fe-Al-BG-$CaZrTi_2O_7$ composite materials of ~ 4.44 g/cm^3, ~ 3.10 g/cm^3, and ~ 3.64 g/cm^3, respectively [41,45]. The XANES spectra were calibrated, normalised, and analysed using the Athena software programme [46].

2.5.2. Si $L_{2,3}$-edge XANES

Si $L_{2,3}$-edge XANES spectra were collected using the Variable Line Spacing-Plane Grating Monochromator (VLS-PGM) beamline located at the Canadian Light Source (CLS), Saskatoon, Saskatchewan [47]. Samples were prepared by brushing ground powder on carbon tape. Spectra were measured under ultra-high vacuum in total fluorescence yield (TFY) mode using a step size of 0.05 eV through the absorption edge. The Si $L_{2,3}$-edge XANES spectra were collected from Fe-Al-BG and Fe-Al-BG-$CaZrTi_2O_7$ composite materials with the attenuation length of photons ~ 0.07 μm and ~ 0.1 μm, respectively. The Si $L_{2,3}$-edge spectra were calibrated by collecting the Si $L_{2,3}$-edge spectrum from a Si wafer with the Si L_3-edge absorption energy set to 99.4 eV [48]. The attenuation length of photons for Si at this energy was calculated using the density of Fe-Al-BG and Fe-Al-BG-$CaZrTi_2O_7$ composite materials from the ICSD at ~ 3.10 g/cm^3 and ~ 3.64 g/cm^3 [41,45]. The XANES spectra were calibrated, normalised, and analysed using the Athena software programme [46].

2.6. Scanning electron microscopy (SEM)

SEM micrographs were collected from powders of Fe-Al-BG, $CaZrTi_2O_7$, and Fe-Al-BG-$CaZrTi_2O_7$ composite materials before and after the leaching tests using a HITACHI SU6600 Scanning Electron Microscope with a secondary electron detector. The samples were mounted on double sided carbon tape and coated with Pt on the sputter coating machine.

3. Results

3.1. Semi-static leaching experiments (ICP-MS analysis)

The elemental concentrations of ions that leached from the proposed wasteform materials into deionised water under semi-static conditions were measured using ICP-MS. Fig. 2a-c illustrate the concentration of ions leached from the Fe-Al-BG, $CaZrTi_2O_7$, and Fe-Al-BG-$CaZrTi_2O_7$ composite materials and were plotted as a function of time. Comparing the ICP-MS data shown in Fig. 2a-c indicate that Fe-Al-BG has lower resistance to aqueous corrosion and released higher concentrations of ions into the leachant solution over 365 days of the leaching experiments. Fig. 2a shows the concentrations of the B and Na ions dissolved from Fe-Al-BG in the leachant solution were considerably higher compared to other ions (i.e., Fe, Al, and Ca). The concentration of most ions leached from the Fe-Al-BG increased in the leachant solution during the first 30 days of the leaching experiments, and gradually decreased or remained constant (within the standard deviation of the measurement) between 30 and 365 days of exposure to deionised water. However, the

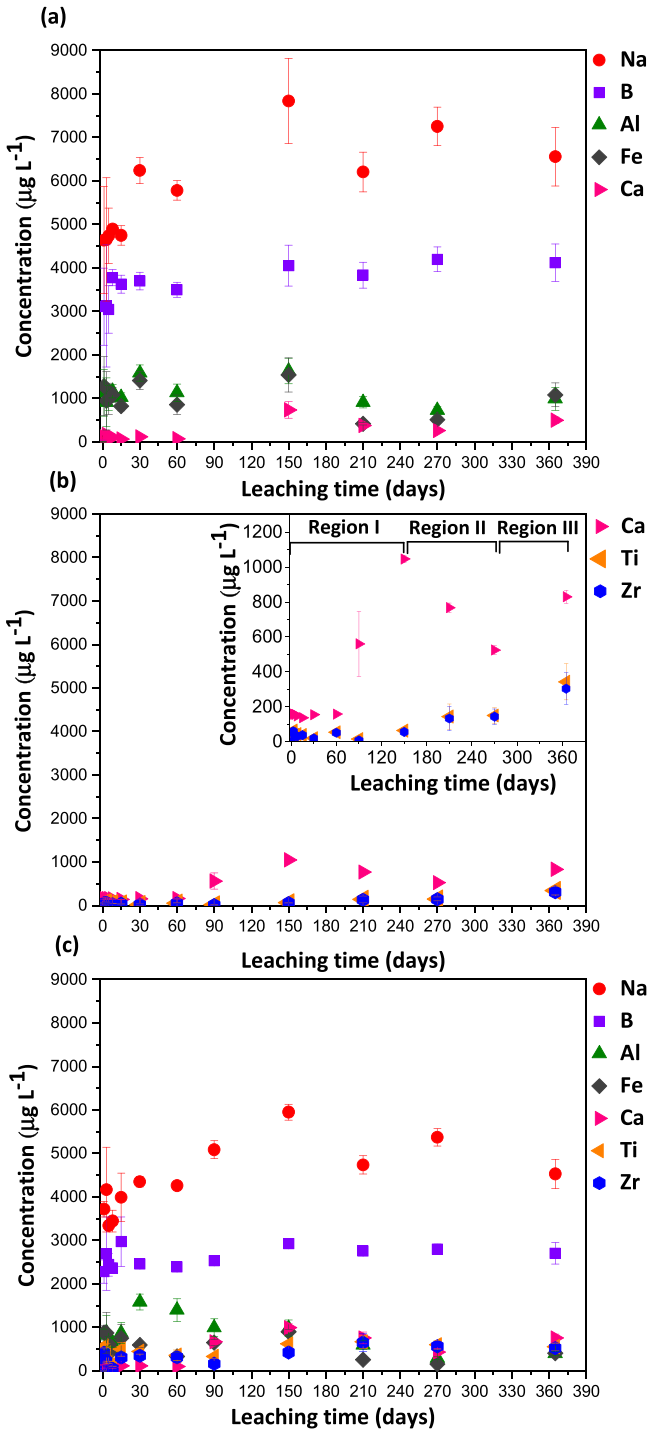

Fig. 2. The ICP-MS results from the unfiltered leachate of (a) Fe-Al-BG, (b) $CaZrTi_2O_7$, and (c) Fe-Al-BG-$CaZrTi_2O_7$ composite materials are plotted as a function of time. The inset in Fig. 2b shows a zoom-in of the concentrations and the three distinct regions.

concentration of Na and Ca reached a maximum after 150 days of being exposed to water likely due to an ion exchange reaction between the Fe-Al-BG network modifying cations and H^+ in water [31,49,50]. The observed leaching trends of Fe-Al-BG suggest a congruent leaching mechanism, in which the ions dissolve into the leachant solution similar to their weight percentage in the starting materials [1,4,30,51]. In this regard, the elemental release of Na and B into the leachant solution was higher compared to Al, Fe, and Ca due to the higher weight percentage of Na and B in the as-synthesised Fe-Al-BG (i.e., 15.3 wt% Na_2O and 17.6 wt% B_2O_3 vs. 2.6 wt% CaO, 7.6 wt% Al_2O_3, and 7.1 wt% Fe_2O_3).

In contrast to the Fe-Al-BG, the $CaZrTi_2O_7$ ceramic exhibited a different dissolution behaviour over 365 days of exposure to deionised water (Fig. 2b). The concentration of Ca ions leached from $CaZrTi_2O_7$ into the leachant solution was considerably higher than Ti and Zr. The concentrations of Ti and Zr in leachate were similar throughout the leaching experiments even though the stoichiometric ratio of Ti and Zr is 2:1 in $CaZrTi_2O_7$. The ICP-MS data suggest that $CaZrTi_2O_7$ has an incongruent dissolution mechanism, which involves the non-stoichiometric release of ions into the leachant solution at different rates [4,52–54]. The dissolution behaviour of $CaZrTi_2O_7$ presented in Fig. 2b can be described by three distinct regions. The first region, referred to as region I, occurs between 1–150 days of the leaching experiment, in which Ca was preferentially dissolved into the leachant solution, and its concentration reached the maximum solubility limit, while Ti and Zr ions had very low solubility and gradually dissolved into the leachant. In the slow-flow rate or static conditions, the concentration of ions dissolved in the leachant solution will increase over time until they reach their solubility limit [4,53,54]. Region II occurs between 150 and 270 days of exposure to deionised water and includes a decrease in the concentration of Ca, while the concentrations of the Zr and Ti ions remained relatively constant. Based on the preferential release of Ca in region I and reaching its saturation point in the leachant solution, we hypothesise that the observed leaching behaviour in region II could be due to the precipitation of an amorphous Ca-containing layer (i.e., Ca hydroxide) on the $CaZrTi_2O_7$ surface, which reduces the leaching of ions into the leachant. This suggestion agrees with several studies that reported the formation of an amorphous layer on the surface of crystalline wasteforms due to the saturation of highly soluble ions in the leachant solution [4,30,39,54]. Finally, the leaching period between 270 and 365 days of exposure (termed region III) shows slight increases in the concentrations of the Ca, Zr, and Ti ions compared to region II. This observation indicates that the suggested Ca hydroxide layer that might be formed previously on the surface of $CaZrTi_2O_7$ has dissolved after 270 days of exposure to deionised water. It should be noted that the amorphous layers formed on the surface of crystalline materials upon exposure to aqueous solutions are thermodynamically unstable and may dissolve or experience phase transformation over time, causing an increase in the concentration of dissolved ions in the leachate [4,30,32,39].

The ICP-MS data from the Fe-Al-BG-$CaZrTi_2O_7$ composite materials indicates that higher concentrations of ions were dissolved into the leachant during the first 30 days of the leaching experiments and gradually decreased or remained constant over the remainder of the 365 days of exposure to deionised water (Fig. 2c). As previously mentioned, the Fe-Al-BG-$CaZrTi_2O_7$ composite materials consists of 40 wt% $CaZrTi_2O_7$ dispersed in 60 wt% of the Fe-Al-BG matrix [55]. Therefore, two simultaneous leaching reactions occurred after the composite materials was exposed to water. The Fe-Al-BG matrix of the Fe-Al-BG-$CaZrTi_2O_7$ composite exhibits a congruent leaching mechanism with the stoichiometric release of ions based on their weight percentage in the as-synthesised Fe-Al-BG. Therefore, higher concentrations of B and Na were dissolved into the leachant solution compared to other ions (i.e., Fe, Al, Si, and Ca) [1,4,31,51]. The concentrations of ions leached from the Fe-Al-BG matrix of the Fe-Al-BG-$CaZrTi_2O_7$ composite was generally lower due to the lower amount of Fe-Al-BG percentage in the composite materials (i.e., 60 wt%) vs. just Fe-Al-BG (i.e., 100 wt%). Moreover, the $CaZrTi_2O_7$ phase in the Fe-Al-BG-$CaZrTi_2O_7$ composite followed the same incongruent leaching mechanism with preferential leaching of highly soluble ions into the leachant solution (Ca> Ti ≈ Zr) that was previously observed for the $CaZrTi_2O_7$ material on its own (cf., Fig. 2b and c) [4,53,54]. The only difference that should be noted is that the concentration of Ca dissolved into the leachant solution from the Fe-Al-BG-$CaZrTi_2O_7$ material was a result of the corrosion of the Fe-Al-BG matrix and the $CaZrTi_2O_7$ phase as both contain Ca. This observation is consistent with the structure of as-synthesised

Fe-Al-BG-$CaZrTi_2O_7$ composite materials, in which the $CaZrTi_2O_7$ crystallites were dispersed in the Fe-Al-BG matrix [55].

The normalised mass loss (N_L) and the normalised leach rate (L_R) of different ions from the Fe-Al-BG, $CaZrTi_2O_7$, and Fe-Al-BG-$CaZrTi_2O_7$ composite materials are shown in Figs. 3 and 4. The normalised mass loss data calculated from the proposed wasteform materials over 365 days of exposure to deionised water followed very similar trends as previously observed for the concentrations of ions that dissolved into the leachant solution (Fig. 3). In the normalised mass loss, the effect of the mass ratio of a leached ion in the solid and reactive surface area of the wasteform on the elemental release has been considered. Therefore, the measured values based on normalised mass loss are more realistic and comparable to the actual chemical durability of wasteform materials compared to the ICP-MS plot of concentrations against time upon exposure to deionised water [36]. Thorpe et al. [36] reported that the normalised mass loss of B from the crushed International Simple Glass (ISG) in ultra-pure water at 25 °C using the PCT method reached ~ 0.25 g m^{-2} over one month of the leaching experiment. Another study performed by Aréna et al. [56] showed that the normalised mass loss of

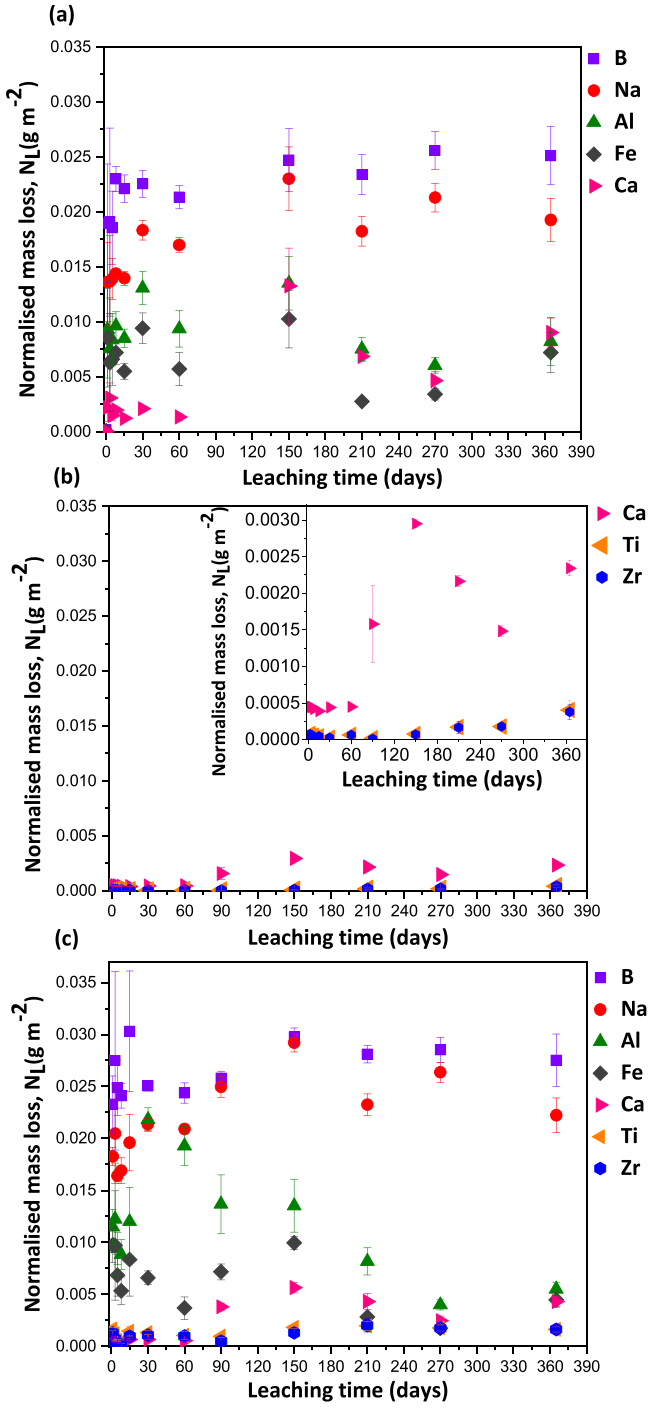

Fig. 3. Normalised mass loss data from (a) Fe-Al-BG, (b) $CaZrTi_2O_7$, and (c) Fe-Al-BG-$CaZrTi_2O_7$ composite materials over 365 days of exposure to water are presented. The inset in Fig. 3b shows a zoom-in of the normalised mass loss from $CaZrTi_2O_7$, as a comparison.

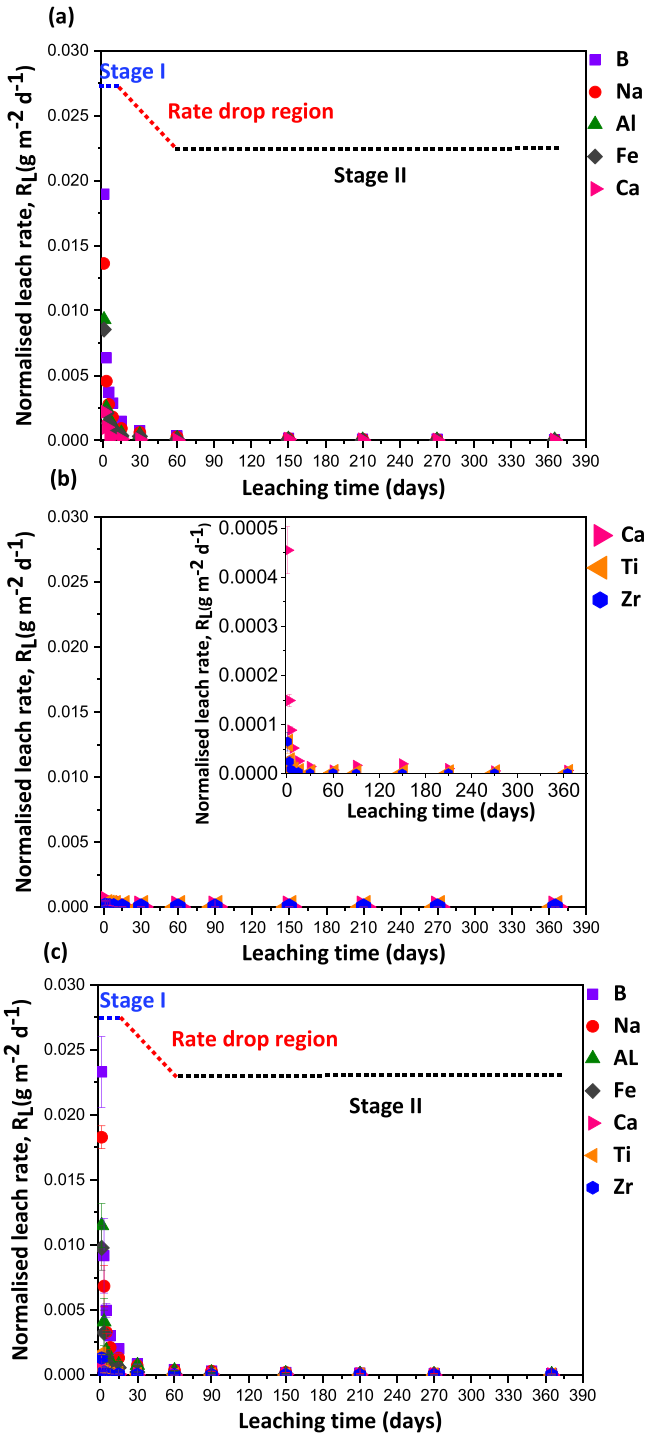

Fig. 4. Normalised leach rates from (a) Fe-Al-BG, (b) $CaZrTi_2O_7$, and (c) Fe-Al-BG-$CaZrTi_2O_7$ composite materials over 365 days of exposure to water are presented. The inset in Fig. 4b shows a zoom-in of the normalised leach rates from $CaZrTi_2O_7$, as a comparison.

B from the ISG powder was around 0.2 g m^{-2} using pure water at an initial pH 7. The normalised mass loss of B from the proposed Fe-Al-BG or Fe-Al-BG-$CaZrTi_2O_7$ composite materials were 0.0251 ± 0.0026 g m^{-2} and 0.0275 ± 0.0025 g m^{-2}, respectively after 365 days of exposure to water. Comparison of the normalised mass loss of B with the reported literature values shows that the leaching performance of Fe-Al-BG is comparable to or better than ISG under similar conditions (Fig. 3a and b).

The normalised leach rates (L_R) of Fe-Al-BG, $CaZrTi_2O_7$, and Fe-Al-BG-$CaZrTi_2O_7$ composite materials over 365 days of exposure to water, along with the log scale of normalised leach rates are shown in Fig. 4 and S3. The leach rates are normalised based on the elemental mass loss of the wasteforms with respect to the ratio of surface area to the leachant volume over time to allow a possible comparison between the leaching rates of each element that dissolved from the wasteform into the leachant solution [51]. Fig. 4a-c indicate the leach rates of Fe-Al-BG, $CaZrTi_2O_7$, and Fe-Al-BG-$CaZrTi_2O_7$ composite materials are higher during 8 days of exposure to deionised water and then decrease considerably between 15 and 30 days followed by a constant rate after 30 days up to 365 days. Fig. 4a shows the initial leaching rates of B, Na, Fe, Al, and Ca from Fe-Al-BG over 15 days of exposure to deionised water are on the order of 10^{-2} g m^{-2} d^{-1}, and significantly decrease to 10^{-6} g m^{-2} d^{-1} over 365 days. The dissolution of the silicate network in glass-based materials occurs through the ion-exchange and hydrolysis reactions of the metal-oxygen bond with water resulting in high leaching rates of ions into the leachant solution in the early leaching stages [4,36, 53,57]. However, the continuous diffusion/dissolution processes of glass components into the leachant results in the saturation of the leachant solution and a formation of an amorphous layer on the surface of the glass-based wasteforms over time. Therefore, this amorphous/protective layer reduces the diffusion of water and ions to and from the glass surface, resulting in a considerable decrease in leaching rates over time [4,36,53,57]. Fig. 4a and S3a indicate the dissolution rates of B and Na from Fe-Al-BG are higher compared to Al, Fe, and Ca ions due to their higher solubility, as well as higher weight percentage of Na and B in the as-synthesised Fe-Al-BG. Due to the high dissolution rates of B and Na from Fe-Al-BG over 365 days of exposure to water, these ions can be considered as the dissolution tracers (i.e., having high solubility) to measure the maximum aqueous corrosion of Fe-Al-BG wasteform during this timeframe [36].

Compared to the normalised leach rates of Fe-Al-BG, the $CaZrTi_2O_7$ ceramic demonstrates a higher chemical durability with much lower normalised leach rates, as shown in Fig. 4b. The normalised leaching rates of Ca, Zr, and Ti ions from $CaZrTi_2O_7$ are on the order of 10^{-4} g m^{-2} d^{-1} over 15 days and fall below 10^{-7} g m^{-2} d^{-1} over 365 days of exposure to deionised water. The higher leaching rate of Ca compared to Zr and Ti ions confirms the preferential dissolution of Ca in water over the entire leaching period (Fig. 4b and S3b). The normalised leach rates of the Fe-Al-BG-$CaZrTi_2O_7$ composite materials exhibit leaching trends that are similar to each of the individual Fe-Al-BG or $CaZrTi_2O_7$ phases. Fig. 4c shows the leach rates of Fe-Al-BG matrix ions of Fe-Al-BG-$CaZrTi_2O_7$ composite (i.e., Na, B, Fe, Al, and Ca) are ~10^{-2} g m^{-2} d^{-1} within 15 days and decrease to 10^{-6} g m^{-2} d^{-1}over 365 days, in which B and Na have higher leaching rates and dissolve more compared to Fe, Al, and Ca ions. Moreover, the initial leach rates of $CaZrTi_2O_7$ phase ions (i.e., Ca, Ti, and Zr) of the Fe-Al-BG-$CaZrTi_2O_7$ composite are on the order of 10^{-3} g m^{-2} d^{-1} during 15 days, and drop to10^{-6} g m^{-2} d^{-1}, while Ca ions maintain higher leaching rates compared to Zr and Ti ions over 365 days of leaching experiment. It should be noted that the Ca leaching rates result from its presence in both the Fe-Al-BG and $CaZrTi_2O_7$ phases. Therefore, B, Na, and Ca ions with high solubility in deionised water can be used as the dissolution tracers for measuring the amount of aqueous dissolution of the Fe-Al-BG-$CaZrTi_2O_7$ composite materials over 365 days of the leaching experiments.

A comparison between the normalised leach rates of Ti and Zr in $CaZrTi_2O_7$ and Fe-Al-BG-$CaZrTi_2O_7$ composite materials during 30 days of the leaching experiment are presented in Table 2. The values of normalised leach rates of Ti and Zr after 365 days of exposure to deionised water are relatively close and represent high corrosion resistance of Ti and Zr whether in the $CaZrTi_2O_7$ or Fe-Al-BG-$CaZrTi_2O_7$ composite materials. This is an important observation that shows not only that the Fe-Al-BG-$CaZrTi_2O_7$ composite material has the combined advantages of both Fe-Al-BG and $CaZrTi_2O_7$ with respect to the immobilisation of nuclear waste elements, but also its aqueous durability is comparable to each of the individual Fe-Al-BG or $CaZrTi_2O_7$ phases [11, 14,19,49].

3.2. Static leaching experiments

Static leaching experiments were performed on the powdered wasteform materials to determine if there were any changes in the long-range order and local chemical environment of the materials after exposure to deionised water. The solid materials were collected at regular intervals (30, 90, 180, 270, and 365 days) and vacuum dried, and structural changes from both the bulk and surface regions of the wasteforms were studied using XRD and XANES.

3.2.1. Bulk analysis of the wasteform materials

3.2.1.1. Structure and phase analysis. The effect of leaching experiments on the structure of $CaZrTi_2O_7$, Fe-Al-BG-$CaZrTi_2O_7$ composite materials, and Fe-Al-BG was investigated using powder XRD before and after exposure to the leachant solution to determine possible changes in long-range structure or formation of any secondary phases during the leaching experiments. The XRD patterns from the as-synthesised $CaZrTi_2O_7$, Fe-Al-BG-$CaZrTi_2O_7$ composite materials, and Fe-Al-BG were compared to the XRD patterns collected from the wasteform materials over 365 days of exposure to deionised water under static conditions (Fig. 5 and Fig. S4). The XRD data collected from the $CaZrTi_2O_7$ and Fe-Al-BG-$CaZrTi_2O_7$ composite materials indicate that there are no secondary phases (at concentrations high enough to be detected by XRD) or changes in the peak widths of these wasteforms after being exposed to water for up to 365 days (Fig. 5a and b). To confirm these observations, the XRD patterns showing the 2θ range of 28 – 35° from $CaZrTi_2O_7$, Fe-Al-BG-$CaZrTi_2O_7$ composite materials, and Fe-Al-BG before, during, and after 365 days of exposure to water are shown in Fig. S4. Moreover, Fig. 5c shows no detectable secondary phases have formed after 365 days exposure of the Fe-Al-BG to water. The XRD analysis confirmed that all three proposed wasteform materials have good structural stability after long-term exposure to an aqueous environment.

Table 2
The normalised leach rates of Ti and Zr in $CaZrTi_2O_7$ and Fe-Al-BG-$CaZrTi_2O_7$ composite after 365 days of the leaching experiment.

Time (days)	$CaZrTi_2O_7$		Fe-Al-BG-$CaZrTi_2O_7$	
	R_L Ti (g.m^{-2}.d^{-1})	R_L Zr (g.m^{-2}.d^{-1})	R_L Ti (g.m^{-2}.d^{-1})	R_L Zr (g.m^{-2}.d^{-1})
1	6.3 (2.1)[a] × 10^{-5}	6.5 (1.9) × 10^{-5}	1.7 (0.1) × 10^{-3}	1.3 (0.2) × 10^{-3}
3	2.5 (0.6) × 10^{-5}	2.4 (0.9) × 10^{-5}	4.1 (2.1) × 10^{-4}	2.4 (1.1) × 10^{-4}
5	9.1 (2.9) × 10^{-6}	8.9 (3.6) × 10^{-6}	1.1 (0.2) × 10^{-4}	4.5 (0.6) × 10^{-5}
8	6.3 (0.6) × 10^{-6}	4.8 (0.3) × 10^{-6}	5.8 (1.9) × 10^{-5}	1.9 (0.9) × 10^{-5}
15	2.9 (0.7) × 10^{-6}	3.1 (1.1) × 10^{-6}	9.8 (3.1) × 10^{-5}	6.4 (2.3) × 10^{-5}
30	7.9 (9.7) × 10^{-7}	7.9 (9.9) × 10^{-7}	4.4 (0.6) × 10^{-5}	3.6 (0.9) × 10^{-5}

[a] Numbers in parentheses represent the standard deviation.

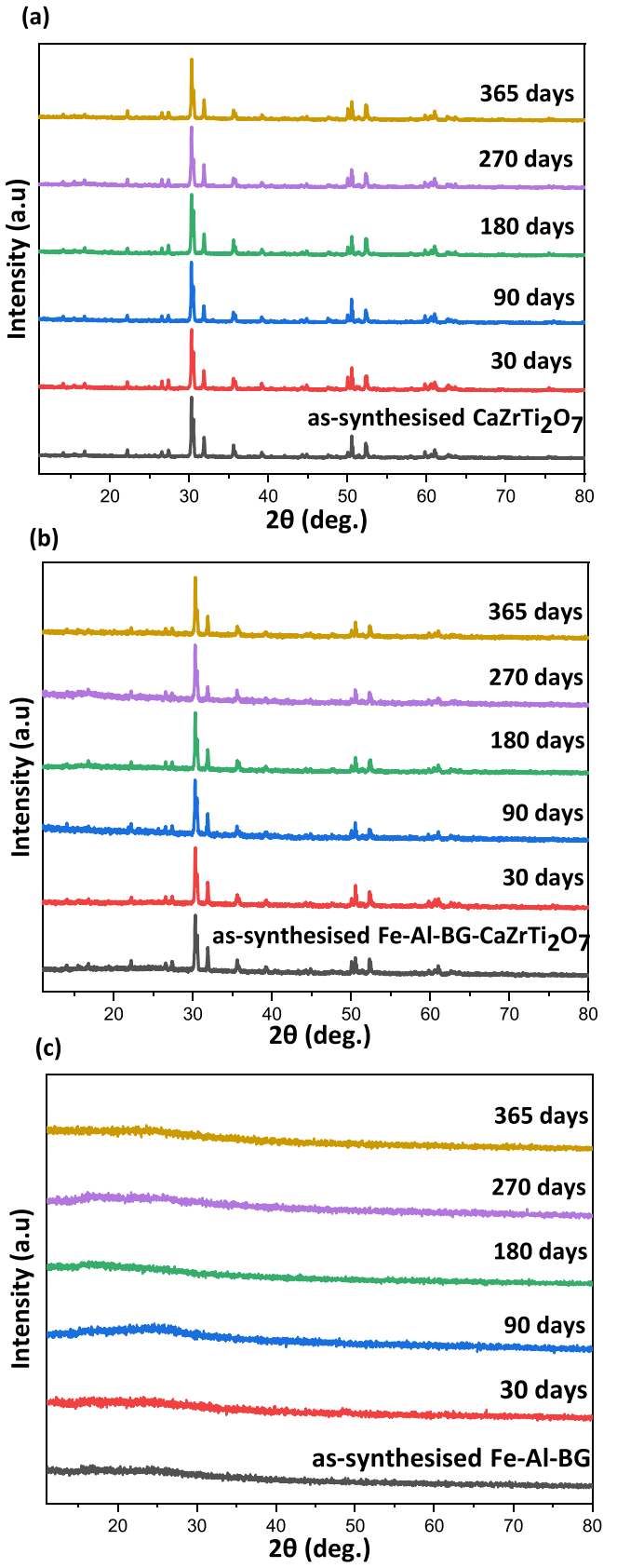

Fig. 5. Powder XRD patterns from the (a) $CaZrTi_2O_7$, (b) Fe-Al-BG-$CaZrTi_2O_7$ composite materials, and (c) Fe-Al-BG before, during, and after 365 days of exposure to water are presented.

3.2.1.2. XANES analysis of $CaZrTi_2O_7$, Fe-Al-BG, and Fe-Al-BG-$CaZrTi_2O_7$ composite. X-ray absorption near-edge spectroscopy (XANES) spectra were collected from the $CaZrTi_2O_7$, Fe-Al-BG, and Fe-Al-BG-$CaZrTi_2O_7$ composite materials to study if the local chemical environment of the ions in these materials changed before, during and after exposure to deionised water for up to 365 days under static leaching conditions.

Ti K-edge XANES spectra were collected from the bulk of $CaZrTi_2O_7$ and Fe-Al-BG-$CaZrTi_2O_7$ composite materials to investigate whether the local chemical environment of the ions located in the bulk of these materials was affected by the leaching experiments. Fig. 6a and b show the normalised Ti K-edge XANES spectra from the $CaZrTi_2O_7$ and Fe-Al-BG-$CaZrTi_2O_7$ composite materials which contain a pre-edge region resulting from 1s → 3d transitions (quadrupolar) and a main-edge region due to 1s → 4p (dipolar) transitions [16,43,58]. Ti adopts a mixture of 5 and 6-coordination environments in the $CaZrTi_2O_7$ structure [3,16,22,43]. As can be seen in Fig. 6a and b, the local chemical environment of Ti remained unchanged in $CaZrTi_2O_7$ and the Fe-Al-BG-$CaZrTi_2O_7$ composite materials before, during and after 365 days of exposure to

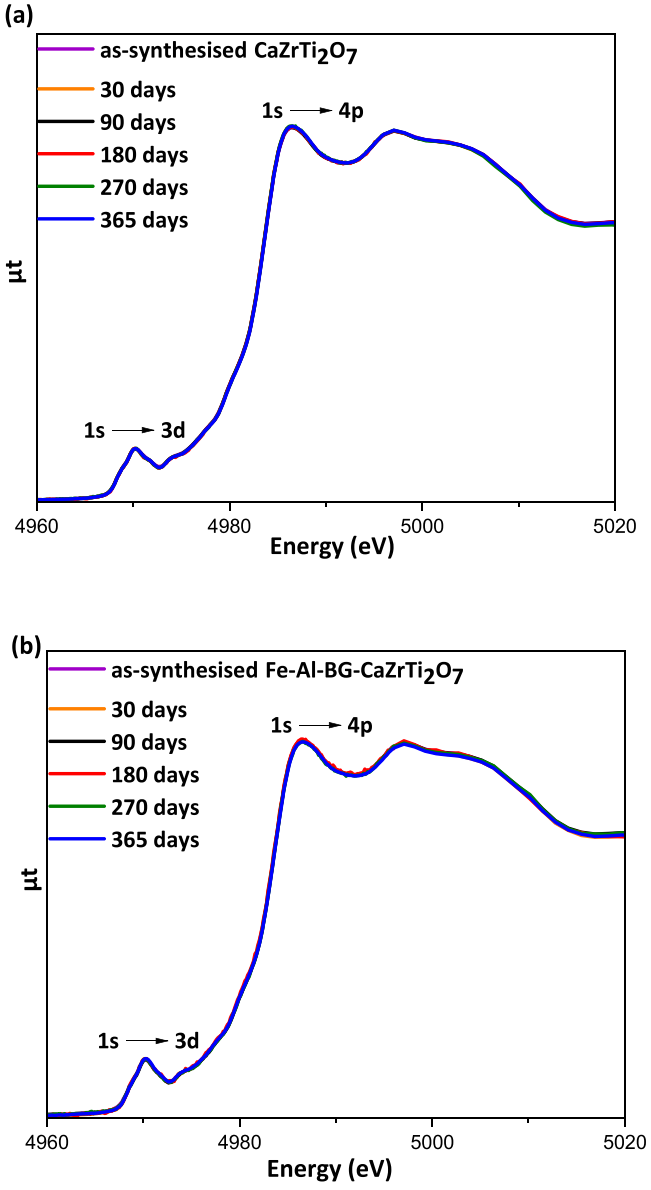

Fig. 6. Normalised Ti K-edge XANES spectra from (a) $CaZrTi_2O_7$ and (b) Fe-Al-BG-$CaZrTi_2O_7$ composite materials over 365 days of exposure to water.

deionised water.

Zr K-edge XANES spectra were collected from the bulk of $CaZrTi_2O_7$ and Fe-Al-BG-$CaZrTi_2O_7$ composite materials to study changes in the local chemical environment of Zr in the bulk of these materials over 365 days of exposure to deionised water (Fig. 7a and b). The normalised Zr K-edge XANES spectra consist of a pre-edge region (quadrupolar, 1s → 4d transition) and a main-edge region (dipolar, 1s → 5p transition) (Fig. 7a and b). The main-edge region of the Zr K-edge XANES spectra can vary depending on changes in the coordination number of Zr^{4+}, which results in a double peak (relates to a lower CN) or a single broad peak (relates to a higher CN) [22,58]. Examination of the normalised Zr K-edge XANES spectra from $CaZrTi_2O_7$ and Fe-Al-BG-$CaZrTi_2O_7$ composite materials shows that the local chemical environment of Zr was consistent in the bulk of these materials before, during, and after 365 days of exposure to deionised water.

Fe K-edge XANES spectra were collected from the bulk of Fe-Al-BG and Fe-Al-BG-$CaZrTi_2O_7$ composite materials to determine whether the oxidation state or coordination environment of Fe in the Fe-Al-BG matrix changed during 365 days of exposure to deionised water. Fig. 8a and b show the normalised Fe K-edge XANES spectra consist of a pre-edge feature because of quadrupolar 1s → 3d transitions and a main-edge feature attributed to dipolar 1s → 4p transitions [16,44]. The presence of a narrow and intense pre-edge peak in both XANES spectra from Fe-Al-BG and Fe-Al-BG-$CaZrTi_2O_7$ composite materials is due to the greater overlap of Fe 3d and Fe 4p states in a structure without a centre of symmetry, which suggests that Fe occupies a lower coordination number (i.e., < 6-coordinate) in the Fe-Al-BG matrix of both materials [16,44]. Moreover, the line shape and absorption energy of the Fe K-edge XANES spectra are consistent with previously reported XANES spectra attributed to Fe adopting a 3 + oxidation state in the bulk phase of the material [16,44]. The normalised Fe K-edge XANES spectra from Fe-Al-BG and Fe-Al-BG-$CaZrTi_2O_7$ composite materials before, during, and after exposure to deionised water for 365 days demonstrate that the local chemical environment of Fe in the bulk region of the Fe-Al-BG and the Fe-Al-BG matrix of Fe-Al-BG-$CaZrTi_2O_7$ composite materials was unaffected by leaching.

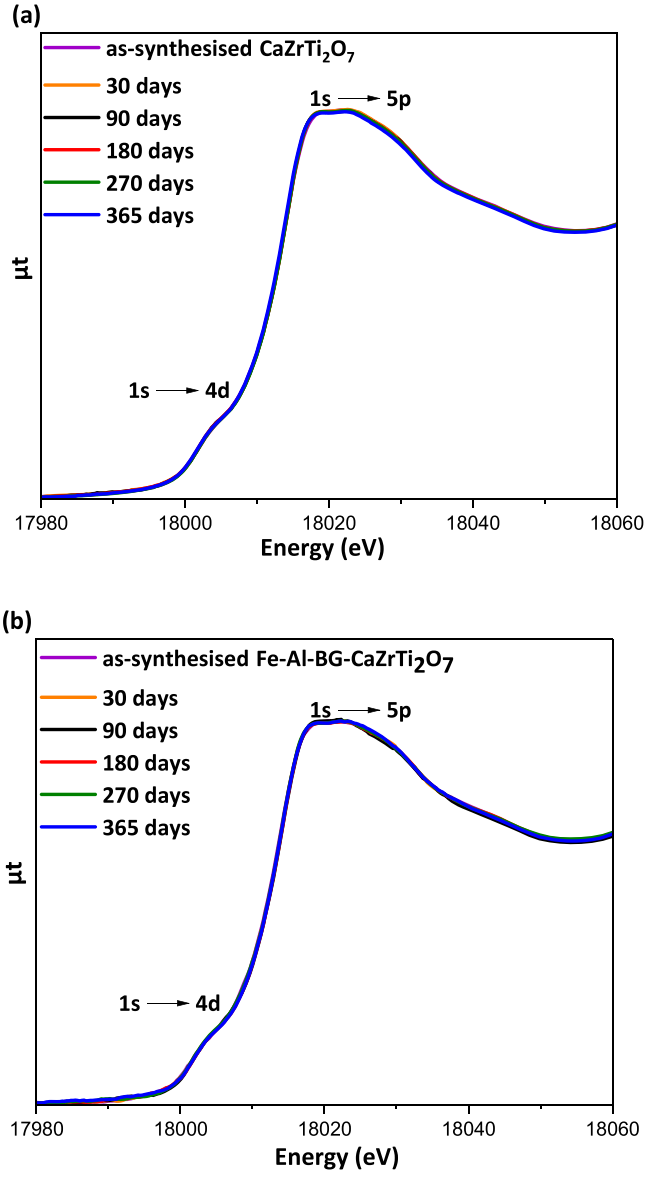

Fig. 7. Normalised Zr K-edge XANES spectra from (a) $CaZrTi_2O_7$ and (b) Fe-Al-BG-$CaZrTi_2O_7$ composite over 365 days of exposure to water.

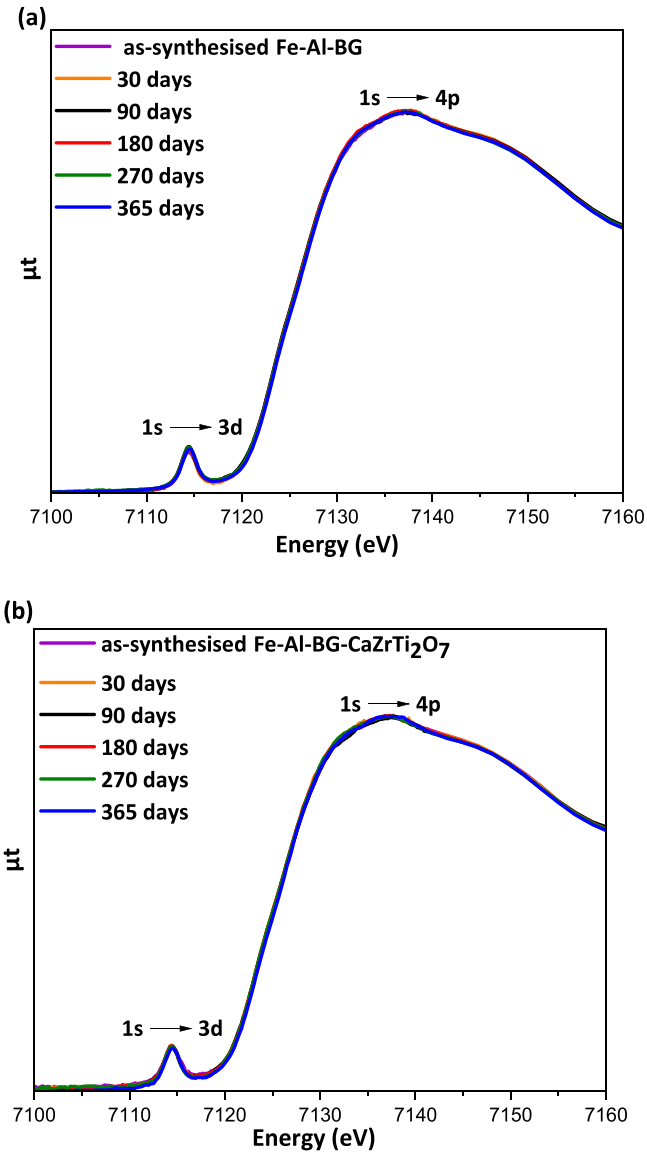

Fig. 8. Normalised Fe K-edge XANES spectra from (a) Fe-Al-BG and (b) Fe-Al-BG-$CaZrTi_2O_7$ composite materials over 365 days of exposure to water are presented.

3.2.2. *Surface analysis of the wasteforms*

3.2.2.1. Si $L_{2,3}$-edge XANES. The Si $L_{2,3}$-edge XANES spectra were

collected from the Fe-Al-BG and Fe-Al-BG-$CaZrTi_2O_7$ composite materials to examine the effect of corrosion on the local chemical environment of Si within the materials before, after, and during 365 days of exposure to deionised water. The Si $L_{2,3}$-edge has a low absorption energy, which allows for the detection of Si-containing surface layers formed because of corrosion. The normalised Si $L_{2,3}$-edge XANES spectra contain two main regions. The lower energy region results from 2p→ 3s transitions, while the higher energy, broader region corresponds to 2p → 3d transitions (Fig. 9a and b) [16,48]. The lower energy feature splits into two peaks ($L_{2,3}$-peaks) due to spin-orbit splitting [48]. Comparing the normalised Si $L_{2,3}$-edge XANES spectra collected from the Fe-Al-BG and Fe-Al-BG-$CaZrTi_2O_7$ composite materials before, during, and after completion of the leaching experiments resulted in the observation of a difference in the low-energy region (i.e., 2p → 3d) of the spectra after only 30 days of exposure to deionised water (Figs. 9a and 9b). A low energy shoulder peak was observed in the lower energy region of the spectra after exposure to deionised water. Several research groups have reported a similar feature in the Si $L_{2,3}$-edge XANES spectra when OH^- group bond with Si^{4+} on material surfaces [59–61]. The presence of this shoulder peak suggests the formation of an amorphous Si-containing surface layer (i.e., Si-OH) due to the dissolution of the silicate network followed by precipitation in the early stages of the leaching experiments [4,31,62]. This observation suggests the dissolution of glass components into the leachant solution through ion exchange or hydrolysis reactions will affect the chemical environment of Si on the surface of Fe-Al-BG or Fe-Al-BG-$CaZrTi_2O_7$ composite materials [4,31,59,62,63].

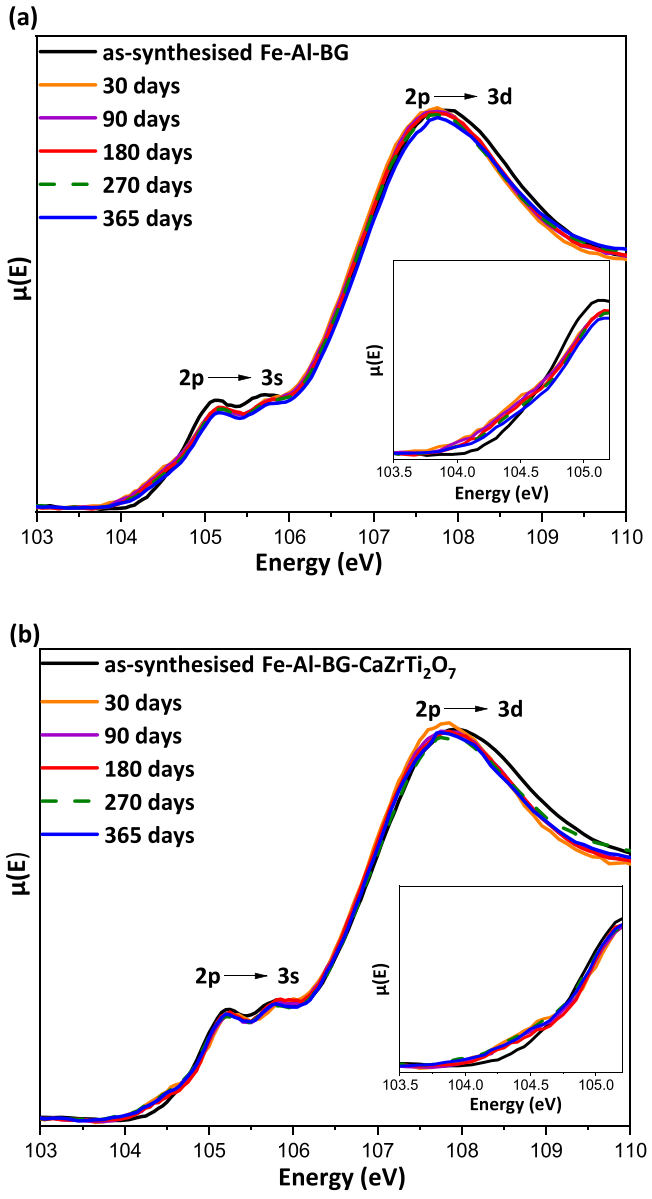

Fig. 9. Normalised Si $L_{2,3}$-edge XANES spectra from (a) Fe-Al-BG and (b) Fe-Al-BG-$CaZrTi_2O_7$ composite materials over 365 days of exposure to water are shown. The inset shows an expanded view of the low energy region of the spectrum (2p → 3s transitions), which highlights the observed shoulder peak in this region.

3.2.2.2. Scanning electron microscopy (SEM) analysis. SEM images were collected from the powder of Fe-Al-BG, $CaZrTi_2O_7$, and Fe-Al-BG-$CaZrTi_2O_7$ composite materials to investigate the effect of aqueous corrosion on the surface morphology of these materials before and after exposure to water. SEM analysis from the powder of Fe-Al-BG and Fe-Al-BG-$CaZrTi_2O_7$ composite materials showed that significant changes had occurred at the surface of these materials after exposure to water compared to the as-synthesised samples (Figs. S5a-d). The surface of as-synthesised Fe-Al-BG showed a distribution of fine particles on the surface of Fe-Al-BG powder, which becomes bigger in size and agglomerated due to the aqueous corrosion with water (Figs. S5a and b). This observation suggests the formation of amorphous secondary precipitates on the surface of the glass, as no secondary crystalline phases (at concentrations high enough to be detected by XRD) were observed in the XRD patterns. Similar surface changes were observed for the Fe-Al-BG-$CaZrTi_2O_7$ composite materials before and after exposure to water, however, for the Fe-Al-BG-$CaZrTi_2O_7$ composite materials, the formation of amorphous secondary precipitates was more uniform and almost the entire surface of Fe-Al-BG-$CaZrTi_2O_7$ composite materials was covered with a precipitation layer (Figs. S5c and d). The formation of amorphous secondary phases on the surface of powder materials is consistent with the observed changes reported in the literature [64–66]. The SEM images from the surface of $CaZrTi_2O_7$ powder did not indicate significant changes in morphology and distribution of fine particles that were presented on the surface of $CaZrTi_2O_7$ powder before and after exposure to water (Figs. S5e and f).

4. Discussion

The result of long-term leaching experiments from this study demonstrated that the corrosion behaviour of Fe-Al-BG-$CaZrTi_2O_7$ composite materials is a combination of the corrosion behaviours of Fe-Al-BG and $CaZrTi_2O_7$ at different rates. The corrosion mechanisms for each of the three types of materials studied here are discussed below.

4.1. Corrosion mechanism of Fe-Al-BG

The leaching behaviour of glass-based materials is a complicated process as the glass surface undergoes phase transformations at different stages over time [4,31,36]. Generally, it is understood that three main stages are involved in the glass dissolution process with different rates on geological time scales, however, the mechanisms responsible for each stage are still being investigated [4,31,36]. Stage I (initial rate) has the highest dissolution rate (known as the forward rate) and occurs at the early leaching process in all glass wasteforms regardless of their composition [31,36]. Two parallel corrosion mechanisms are responsible during stage I of the glass dissolution. (1) ion-exchange reaction between highly mobile ions (i.e., alkali ions) in the glass and H^+ from water, and (2) a hydrolysis reaction of network-forming ions with water and breaking of the bridging Si-O-M bonds (M= Si, B, Al, or Fe) in the glass structure [5,14,31,36,49,63]. Before stage II begins, there is a transitional region in the glass dissolution mechanism that is referred to as the rate drop region, in which the leach rates slowly decrease due to the continuous dissolution of the glass network and the saturation of the

leachant solution, particularly with respect to Si [5,14,31,36,49]. The saturation of the leachant in the rate drop region leads to the precipitation of dissolved species (i.e., Si-OH), and the formation of a protective layer on the glass surface [5,6,14,31,36,49]. As the surface layer has been formed, stage II of glass dissolution known as the residual rate, begins in which the dissolution rates remain constant or decrease slowly over time [5,6,14,31,36,49]. The nearly constant leach rate during stage II is because ions need to diffuse through the surface layer to leach from the glass into the leachant solution [5,6,14,31,36,49]. Finally, stage III, known as the resumption rate, can be observed in some types of glasses over a long-term exposure to deionised water (i.e., years) causes the dissolution rate to increase [6,31,36]. Although the reaction mechanisms of the resumption rate are still vague, two reasons are generally accepted for the increase of leaching rates in stage III: (i) the precipitation of metal-silicate phases, especially in glass wasteforms with high concentrations of Ca and Al, leading to a decrease of the Si concentration in the leachate, which causes the glass network to further dissolve or (ii) change in the chemistry or morphology (cracking or dissolving) properties of the amorphous protective layer formed on the surface of glass over time, which can increase the glass dissolution rate [4,6,31,36]. The time scale of glass dissolution at each stage can vary depending on the environmental conditions (e.g., temperature, pH), leachant composition, and glass composition [4,6,31,36].

The Fe-Al-BG investigated in this study has shown stages I and II of the glass dissolution mechanism as described above over a period of 365 days of exposure to deionised water under semi-static conditions. The ICP-MS data from Fe-Al-BG indicated that the Fe-Al-BG material achieved stage I (the maximum rate at a given temperature) over 15 days, followed by a rate drop region between 15 and 60 days, and reached the residual rate (stage II) after 60 days of exposure to deionised water. During stage II of the Fe-Al-BG dissolution (between 60 and 365 days), the concentration of dissolved species slowly decreased or remained constant. The relatively constant concentration of ions in stage II could be due to the formation of a protective surface layer during the rate drop region, as discussed above (Fig. 4a). The analysis of the Si $L_{2,3}$-edge XANES spectra from the Fe-Al-BG materials clearly demonstrated that the surface chemistry of Fe-Al-BG changed before, over, and after exposure to deionised water. Moreover, the SEM analysis suggested that an amorphous precipitate has been formed on the surface of Fe-Al-BG after 365 days of exposure to water. However, the analysis of Fe K-edge XANES spectra and XRD data have shown no change in the bulk of Fe-Al-BG over 365 days of exposure to deionised water (i.e., only changes to the surface of the material was observed). The absence of stage III in the corrosion mechanisms of Fe-Al-BG indicates that the suggested protective surface layer was stable during this timeframe (i.e., 365 days).

4.2. Corrosion mechanism of $CaZrTi_2O_7$

The chemical durability of crystalline oxide materials upon contact with aqueous environments strongly depends on the strength of the metal-oxygen bonds [4,53]. The dissolution of crystalline materials starts with the breaking of metal-oxygen bonds through the chemical reaction with water molecules at the surface and the release of ions into leachant solution until the concentration of the dissolved ions reaches the solubility limit [4,30,53,54]. The corrosion mechanism of crystalline materials can be considered congruent (i.e., leach rate of ions are equal to the stoichiometric ratio of ions in as-synthesised material) or incongruent with a preferential and non-stoichiometric release of ions into the leachant solution [3,4,19,26,54]. The ICP-MS data from $CaZrTi_2O_7$ after being exposed to water for 365 days demonstrated a preferential release of Ca ions over Zr and Ti ions. Two factors are likely responsible for the incongruent dissolution behaviour of crystalline materials: (1) the solubility of ions into the leachant and (2) the strength of the metal-oxygen bonds [3,4,6,53]. The low leaching rates of Zr and Ti and the higher leaching rate of Ca suggest that the ionic potential (i.e., the ratio of charge to ionic radius with respect to the coordination number) influences the breaking of these metal-oxygen bonds [4,6]. In this case, the lower ionic potential of 8-coordinate Ca^{2+} (2.86×10^{-19} C/Å) compared to 7-coordinate Zr^{4+} (8.21×10^{-19} C/Å) and 5-coordinate Ti^{4+} (12.55×10^{-19} C/Å) or 6-coordinate Ti^{4+} (10.57×10^{-19} C/Å) results in a higher dissolution rate of Ca ions compared to Ti or Zr [3,4,6,67]. The higher leaching of Ca ions into the leachant solution leads to the saturation of the leachate with respect to Ca and possible formation of an amorphous precipitate (a hydrated Ca-containing layer) on the surface of $CaZrTi_2O_7$ after 150 days of exposure to deionised water (region II in Fig. 2b) [4,30,39,54]. This suggestion agrees with the constant concentrations of Ti and Zr ions and decreasing Ca concentration in the leachate between 150 and 270 days (region II) of exposure to deionised water [3,4]. However, it is possible that this layer (if any) partially dissolved due to the slightly higher concentration of Ca, Zr, and Ti ions after 270 days up to 365 days (region III), and no significant changes have been observed in the SEM images from $CaZrTi_2O_7$ after 365 days of exposure to water. The results of XRD data and normalised Ti K- and Zr K-edge XANES spectra from $CaZrTi_2O_7$ revealed that the bulk local chemical environment of these ions in $CaZrTi_2O_7$ remained unchanged indicating that any changes would only be present at the ceramic-solution interface (i.e., the surface).

4.3. Corrosion mechanism of the Fe-Al-BG-$CaZrTi_2O_7$ composite materials

In the Fe-Al-BG-$CaZrTi_2O_7$ composite materials, two different dissolution mechanisms are responsible for the leaching of ions into the leachant solution. The results of this study demonstrated that the Fe-Al-BG and $CaZrTi_2O_7$ phases in the Fe-Al-BG-$CaZrTi_2O_7$ composite materials undergo dissolution processes at different rates [16,48,68]. The Fe-Al-BG matrix of the Fe-Al-BG-$CaZrTi_2O_7$ composite materials has a congruent dissolution mechanism with stoichiometric leaching of ions (i.e., B, Na, Fe, Al, and Ca) into the leachant, while the $CaZrTi_2O_7$ phase shows a non-stoichiometric release of ions (i.e., Ca, Zr, and Ti) into the leachant (an incongruent mechanism) [3,4,7,13,18,69]. The Fe-Al-BG matrix has higher dissolution rates and dissolves quicker into the leachant solution because of having highly mobile ions and a less ordered structure, whereas the $CaZrTi_2O_7$ phase dissolves slowly into the leachant solution [13,14,18,50,53]. The corrosion mechanism of the Fe-Al-BG-$CaZrTi_2O_7$ composite materials is likely controlled by two main stages with different rates over 365 days of exposure to deionised water. Stage I (initial rate) occurs between 1–15 days of the leaching experiments, having the highest leaching rates due to the simultaneous ion exchange and hydrolysis reactions of the Fe-Al-BG matrix and ionic dissociation of the $CaZrTi_2O_7$ phase [13,14,18,50,53]. Moreover, similar to the leaching rate data for Fe-Al-BG, there is a rate drop region before stage II, in which the leach rates slowly decreased between 15 and 60 days of the leaching experiments likely due to the formation of an amorphous Si-containing surface layer. Stage II (residual rate) begins after the formation of the amorphous surface layer, which limits the transport of ions to and from the leachant and kept the concentration of ions nearly constant for the remainder of the leaching experiment [6,7,13,18,53]. The formation of the amorphous surface precipitate due to the dissolution of Fe-Al-BG matrix was suggested above based on the analysis of SEM images and the Si $L_{2,3}$-edge XANES spectra (Figs. S5c,d, and 9b). The presence of this amorphous surface layer could likely protect the bulk of $CaZrTi_2O_7$ phase of the Fe-Al-BG-$CaZrTi_2O_7$ composite materials from further aqueous corrosion since the ions need to pass through this protective layer to be leached into the leachant [7,13,18,53,69,70]. The normalised leach rates of Ti and Zr in $CaZrTi_2O_7$ (on the order of 10^{-5} - 10^{-7} g m^{-2} d^{-1}) vs. the Fe-Al-BG-$CaZrTi_2O_7$ composite materials (on the order of 10^{-3} - 10^{-5} g m^{-2} d^{-1}) reported in Table 2 indicated the low solubility of these ions during the first 30 days of exposure to deionised water. The observed difference could be due to the composition of as-synthesised $CaZrTi_2O_7$ compared to as-synthesised

Fe-Al-BG-$CaZrTi_2O_7$ composite materials. The crystalline as-synthesised $CaZrTi_2O_7$ is a single-phase ceramic, whereas the as-synthesised Fe-Al-BG-$CaZrTi_2O_7$ composite materials have a multiphase structure with 40 wt% of $CaZrTi_2O_7$ dispersed in the Fe-Al-BG matrix. Grain boundaries that were formed in the Fe-Al-BG-$CaZrTi_2O_7$ composite materials due to the presence of $CaZrTi_2O_7$ phase in the Fe-Al-BG matrix may experience preferential dissolution resulting in slightly higher leach rates of Ti and Zr ions in the early leaching stages [4,30,31,39]. The analysis of the Ti K- and Zr K-edge XANES spectra and XRD data confirmed that the bulk local chemical environment of these ions in Fe-Al-BG-$CaZrTi_2O_7$ composite materials as well as the long-range structure remained unaffected over 365 days of exposure to water.

5. Conclusion

The long-term aqueous corrosion behaviour of Fe-Al-BG-$CaZrTi_2O_7$ composite materials was investigated under static and semi-static conditions and compared to that of candidate $CaZrTi_2O_7$ wasteform and Fe-Al-BG that is currently being used for nuclear waste sequestration [3,8,9,17,20,31,36]. This study has demonstrated that $CaZrTi_2O_7$, Fe-Al-BG, and Fe-Al-BG-$CaZrTi_2O_7$ composite materials have different dissolution mechanisms depending on their structure (i.e., crystalline vs. amorphous). The semi-static leaching experiments revealed that the Fe-Al-BG-$CaZrTi_2O_7$ composite materials have a leaching mechanism that is a combination of individual Fe-Al-BG and $CaZrTi_2O_7$ dissolution behaviours. This is an important finding as different corrosion mechanism of the Fe-Al-BG-$CaZrTi_2O_7$ composite phases lead to higher leach rates of the Fe-Al-BG matrix, and consequently the formation of an amorphous surface layer. The ICP-MS result after 365 days of the semi-static leaching experiments showed the leach rates of the key elements of Fe-Al-BG-$CaZrTi_2O_7$ composite materials (i.e., Ti and Zr) were comparable and close to the pure $CaZrTi_2O_7$. The structural analysis of the bulk of Fe-Al-BG-$CaZrTi_2O_7$ composite materials (i.e., XRD and high energy XANES data) indicated that this proposed material has good chemical durability and has shown no change after 365 days of exposure to deionised water. Moreover, the presence of an amorphous precipitate on the surface of Fe-Al-BG and Fe-Al-BG-$CaZrTi_2O_7$ composite materials was observed by SEM and Si $L_{2,3}$-edge XANES analyses after these materials were exposed to water. The formation of a protective surface layer would likely reduce the dissolution of the $CaZrTi_2O_7$ phase of the Fe-Al-BG-$CaZrTi_2O_7$ composite materials over time. Although the Fe-Al-BG-$CaZrTi_2O_7$ composite has demonstrated good structural stability and chemical durability, significant efforts should be devoted to using different leaching test conditions (i.e., different leachant solutions, pH, and temperatures) for further evaluation of its long-term dissolution behaviour. Understanding the leaching mechanism of various composite materials and how they could corrode upon exposure to deionised water over time is essential to investigate whether the composite materials can be considered as potential wasteform candidates for future nuclear waste disposal management.

CRediT authorship contribution statement

Mikhchian Mehrnaz: Writing – original draft, Visualization, Methodology, Investigation, Formal analysis, Data curation, Conceptualization. **Grosvenor Andrew:** Writing – review & editing, Validation, Supervision, Resources, Project administration, Methodology, Funding acquisition, Data curation, Conceptualization.

Declaration of Competing Interest

The authors declare that they have no known competing financial interests or personal relationships that could have appeared to influence the work reported in this paper.

Data availability

Data will be made available on request.

Acknowledgements

This work was funded by the Natural Sciences and Engineering Research Council (NSERC) of Canada through a discovery grant awarded to APG. Dr. Mark Button is thanked for collecting the ICP-MS data located at the Fipke Laboratory for Trace Element Research (FiLTER), University of British Columbia, Okanagan campus. Prof. Lee Wilson (Department of Chemistry, University of Saskatchewan) is thanked for conducting the specific surface area measurements. The Saskatchewan Structural Sciences Centre (SSSC) at the University of Saskatchewan is thanked for providing access to the Rigaku Ultima IV powder X-Ray Diffractometer. Canada Foundation for Innovation, Natural Sciences and Engineering Research Council of Canada and the University of Saskatchewan support research at the SSSC. Drs. George Sterbinsky and Tianpin Wu are thanked for their support in carrying out XANES experiments using the 9BM beamline at the APS, and Dr. Lucia Zuin is thanked for her help in carrying out XANES experiments using the VLS-PGM beamline at the CLS. The CLS is supported by NSERC, the National Research Council of Canada, the Canadian Institutes of Health Research, the Province of Saskatchewan, Western Economic Diversification Canada, and the University of Saskatchewan. Sector 9 (CLS@APS) facilities at the Advanced Photon Source are supported by the US Department of Energy - Basic Energy Sciences, the Canadian Light Source and its funding partners, and the Advanced Photon Source. Use of the Advanced Photon Source, an Office of Science User Facility operated for the U.S. Department of Energy (DOE) Office of Science by Argonne National Laboratory, was supported by the U.S. DOE under Contract No. DE-AC02–06CH11357.

Appendix A. Supporting information

Supplementary data associated with this article can be found in the online version at doi:10.1016/j.corsci.2024.111831.

References

[1] L.L. Hench, D.E. Clark, E. Lue Yen-Bower, Corrosion of glasses and glass-ceramics, Nucl. Chem. Waste Manag. 1 (1980) 59–75, https://doi.org/10.1016/0191-815X(80)90029-7.
[2] C.Z. Liao, K. Shih, W.E. Lee, Crystal Structures of Al-Nd codoped zirconolite derived from glass matrix and powder sintering, Inorg. Chem. 54 (2015) 7353–7361, https://doi.org/10.1021/acs.inorgchem.5b00847.
[3] L.R. Blackburn, D.J. Bailey, S.K. Sun, L.J. Gardner, M.C. Stennett, C.L. Corkhill, N. C. Hyatt, Review of zirconolite crystal chemistry and aqueous durability, Adv. Appl. Ceram. 120 (2021) 69–83, https://doi.org/10.1080/17436753.2021.1877596.
[4] G.S. Frankel, J.D. Vienna, J. Lian, J.R. Scully, S. Gin, J.V. Ryan, J. Wang, S.H. Kim, W. Windl, J. Du, A comparative review of the aqueous corrosion of glasses, crystalline ceramics, and metals, npj Mater. Degrad. 17 (1) (2018) 15, https://doi.org/10.1038/s41529-018-0037-2.
[5] T. Geisler, A. Janssen, D. Scheiter, T. Stephan, J. Berndt, A. Putnis, Aqueous corrosion of borosilicate glass under acidic conditions: a new corrosion mechanism, J. Non Cryst. Solids 356 (2010) 1458–1465, https://doi.org/10.1016/j.jnoncrysol.2010.04.033.
[6] S. Gin, A. Abdelouas, L.J. Criscenti, W.L. Ebert, K. Ferrand, T. Geisler, M. T. Harrison, Y. Inagaki, S. Mitsui, K.T. Mueller, J.C. Marra, C.G. Pantano, E. M. Pierce, J.V. Ryan, J.M. Schofield, C.I. Steefel, J.D. Vienna, An international initiative on long-term behavior of high-level nuclear waste glass, Mater. Today 16 (2013) 243–248, https://doi.org/10.1016/j.mattod.2013.06.008.
[7] L. Wu, H. Li, X. Wang, J. Xiao, Y. Teng, Y. Li, Effects of Nd content on structure and chemical durability of zirconolite–barium borosilicate glass-ceramics, J. Am. Ceram. Soc. 99 (2016) 4093–4099, https://doi.org/10.1111/jace.14440.
[8] M.I. Ojovan, W.E. Lee, Glassy wasteforms for nuclear waste immobilization, Metall. Mater. Trans. A 42 (2011) 837–851, https://doi.org/10.1007/s11661-010-0525-7.
[9] L. Wang, T. Liang, Ceramics for high level radioactive waste solidification, J. Adv. Ceram. 1 (2012) 194–203, https://doi.org/10.1007/s40145-012-0019-8.
[10] J.W. Shade, Comparison of glass and ceramic leaching behavior by natural analogs, Nucl. Chem. Waste Manag. 2 (1981) 219–228, https://doi.org/10.1016/0191-815X(81)90019-X.

[11] M.R.A. Rafiuddin, Structural and spectroscopic investigation of hydrous and anhydrous rare earth phosphates, University of Saskatchewan, 2017.
[12] G. Donato, Development of glass-ceramic composites by one-step synthesis methods, University of Saskatchewan, 2019.
[13] A. Doret, N. Pellerin, M. Allix, S. Pellerin, V. Léna, K. Perrigaud, D. Massiot, Influence of alteration solutions on the chemical durability of the zerodur® glass-ceramic: structural investigation, Int. J. Appl. Ceram. Technol. 12 (2015) 811–822, https://doi.org/10.1111/ijac.12270.
[14] J.S. McCloy, A. Goel, Glass-ceramics for nuclear-waste immobilization, MRS Bull. 42 (2017) 233–238, https://doi.org/10.1557/mrs.2017.8.
[15] A. Salamat, P.F. McMillan, S. Firth, K. Woodhead, A.L. Hector, G. Garbarino, M. C. Stennett, N.C. Hyatt, Structural transformations and disordering in zirconolite ($CaZrTi_2O_7$) at high pressure, Inorg. Chem. 52 (2013) 1550–1558, https://doi.org/10.1021/ic302346g.
[16] E.R. Aluri, A.P. Grosvenor, A study of the electronic structure and structural stability of $Gd_2Ti_2O_7$ based glass-ceramic composites, RSC Adv. 5 (2015) 80939–80949, https://doi.org/10.1039/C5RA10720B.
[17] D. Caurant, P. Loiseau, O. Majérus, V. Aubin-Chevaldonnet, I. B. and A. Q. Quintas, Glasses, Glass-Ceramics and Ceramics for Immobilization of Highly Radioactive Nuclear Wastes, Nova Science Publishers, Paris, 2009.
[18] Y. Zhang, L. Kong, I. Karatchevtseva, R.D. Aughterson, D.J. Gregg, G. Triani, Development of brannerite glass-ceramics for the immobilization of actinide-rich radioactive wastes, J. Am. Ceram. Soc. 100 (2017) 4341–4351, https://doi.org/10.1111/jace.14975.
[19] Y. Zhang, M.W.A. Stewart, H. Li, M.L. Carter, E.R. Vance, S. Moricca, Zirconolite-rich titanate ceramics for immobilisation of actinides – Wasteform/HIP can interactions and chemical durability, J. Nucl. Mater. 395 (2009) 69–74, https://doi.org/10.1016/j.jnucmat.2009.09.019.
[20] G.R. Lumpkin, Ceramic waste forms for actinides, Elements 2 (2006) 365–372, https://doi.org/10.2113/gselements.2.6.365.
[21] C. Liao, C. Liu, M. Su, K. Shih, Quantification of the partitioning ratio of minor actinide surrogates between zirconolite and glass in glass-ceramic for nuclear waste disposal, Inorg. Chem. 56 (2017) 9913–9921, https://doi.org/10.1021/acs.inorgchem.7b01425.
[22] S. McCaugherty, A.P. Grosvenor, Low-temperature synthesis of $CaZrTi_2O_7$ Zirconolite-type materials using ceramic, coprecipitation, and sol-gel methods, J. Mater. Chem. C 7 (2019) 177–187, https://doi.org/10.1039/C8TC04560G.
[23] H.J. Rossell, Zirconolite-a fluorite-related superstructure, Nature 283 (1980) 282–283, https://doi.org/10.1038/283282a0.
[24] K. Momma, F.J. Izumi, M. Newville, VESTA: a three-dimensional visualization system for electronic and structural analysis, J. Appl. Crystallogr. 41 (2008) 653–658, https://doi.org/10.1107/S0021889808012016.
[25] D.M. Strachan, Results from long-term use of the MCC-1 static leach test method, Nucl. Chem. Waste Manag. 4 (1983) 177–188, https://doi.org/10.1016/0191-815X(83)90008-6.
[26] National Research Council, National research council (U.S.) committee on waste forms technology and performance, National research council (U.S.) nuclear and radiation studies board, waste form. Testing, in Waste Forms Technology and Performance: Final Report, National Academies Press,, 2011, pp. 119–152.
[27] D.M. Strachan, B.O. Barnes, R.P. Turcotte, Standard leach tests for nuclear waste materials, conference: 3. annual meeting of the materials research society, Boston, MA, USA, 1980.
[28] B.M. Clark, P. Tumurugoti, S.K. Sundaram, J.W. Amoroso, J.C. Marra, Preparation and characterization of multiphase ceramic designer waste forms, Sci. Rep. 11 (2021) 1–10, https://doi.org/10.1038/s41598-021-84014-1.
[29] ASTM International, ASTM-C1662–18. Standard practice for measurement of the glass dissolution rate using the single-pass flow-through test method, https://www.astm.org/c1662–18.html, 2018.
[30] R.C. Ewing, W. Lutze, Radioactive waste forms for the future, North-Holland, 1988.
[31] C.M. Jantzen, K.G. Brown, J.B. Pickett, Durable glass for thousands of years, Int. J. Appl. Glass Sci. 1 (2010) 38–62, https://doi.org/10.1111/j.2041-1294.2010.00007.x.
[32] D. Ngo, H. Liu, H. Kaya, Z. Chen, S.H. Kim, Dissolution of silica component of glass network at early stage of corrosion in initially silica-saturated solution, J. Am. Ceram. Soc. 11 (2019) 6649–6657, https://doi.org/10.1111/jace.16550.
[33] Active Standard ASTM C1220-17, Standard test method for static leaching of monolithic waste forms for disposal of radioactive waste, Environ. Prot. 14 (1987) 1–22, https://webstore.ansi.org/standards/astm/astmc122017.
[34] N. Dacheu, N. Clavier, R. Podor, Versatile monazite: resolving geological records and solving challenges in materials science. monazite as a promising long-term radioactive waste matrix: benefits of high-structural flexibility and chemical durability, Am. Mineral. 98 (2013) 833–847, https://doi.org/10.2138/am.2013.4307.
[35] C.Q. Buckwalter, L.R. Pederson, G.L. McVay, The effects of surface area to solution volume ratio and surface roughness on glass leaching, J. Non-Cryst. Solids 49 (1982) 397–412, https://doi.org/10.1016/0022-3093(82)90135-1.
[36] C.L. Thorpe, J.J. Neeway, C.I. Pearce, R.J. Hand, A.J. Fisher, S.A. Walling, N. C. Hyatt, A.A. Kruger, M. Schweiger, D.S. Kosson, C.L. Arendt, J. Marcial, C. L. Corkhill, Forty years of durability assessment of nuclear waste glass by standard methods, npj Mater. Degrad. 5 (2021) 1–28, https://doi.org/10.1038/s41529-021-00210-4.
[37] L.D. Wilson, M.H. Mohamed, J.V. Headley, Surface area and pore structure properties of urethane-based copolymers containing β-cyclodextrin, J. Colloid Interface Sci. 357 (2011) 215–222, https://doi.org/10.1016/j.jcis.2011.01.081.
[38] X. Zhao, Y. Teng, L. Wu, Y. Huang, J. Ma, G. Wang, Chemical durability and leaching mechanism of $Ce_{0.5}Eu_{0.5}PO_4$ ceramics: effects of temperature and pH values, J. Nucl. Mater. 466 (2015) 187–193, https://doi.org/10.1016/j.jnucmat.2015.08.012.
[39] M.R. Rafiuddin, A.P. Grosvenor, An investigation of the chemical durability of hydrous and anhydrous rare-earth phosphates, J. Nucl. Mater. 509 (2018) 631–643, https://doi.org/10.1016/j.jnucmat.2018.07.039.
[40] W. Kraus, G. Nolze, Powder cell– a program for the representation and manipulation of crystal structures and calculation of the resulting X-ray powder patterns, J. Appl. Crystallogr. 29 (1996) 301–303, https://doi.org/10.1107/S0021889895014920.
[41] A. Belsky, M. Hellenbrandt, V.L. Karen, P. Luksch, New developments in the inorganic crystal structure database (ICSD): accessibility in support of materials research and design, Acta Cryst. 58 (2002) 364–369, https://doi.org/10.1107/S0108768102006948.
[42] S.M. Heald, D.L. Brewe, E.A. Stern, K.H. Kim, F.C. Brown, D.T. Jiang, E.D. Crozier, R.A. Gordon, XAFS and micro-XAFS at the PNC-CAT beamlines, J. Synchrotron Radiat. 6 (1999) 347–349, https://doi.org/10.1107/S090904959801677X.
[43] M.W. Gaultois, A.P. Grosvenor, XANES and XPS investigations of $(TiO_2)_x(SiO_2)_{1-x}$: the contribution of final-state relaxation to shifts in absorption and binding energies, J. Mater. Chem. 21 (2011) 1829–1836, https://doi.org/10.1039/C0JM03464A.
[44] J.A. Sigrist, M.W. Gaultois, A.P. Grosvenor, Investigation of the Fe K-edge XANES spectra from $Fe_{1-x}Ga_xSbO_4$: local versus nonlocal excitations, J. Phys. Chem. A. 115 (2011) 1908–1912, https://doi.org/10.1021/jp111520r.
[45] B.L. Henke, E.M. Gullikson, J.C. Davis, X-ray interactions: photoabsorption, scattering, transmission, and reflection at E=50-30000 eV, Z=1-92, . Data Nucl. Data Tables 54 (1993) 181–342, https://doi.org/10.1006/adnd.1993.1013.
[46] B. Ravel, M. Newville, ATHENA, ARTEMIS, HEPHAESTUS: data analysis for X-ray absorption spectroscopy using IFEFFIT, J. Synchrotron Radiat. 12 (2005) 537–541, https://doi.org/10.1107/S0909049505012719.
[47] Y.F. Hu, L. Zuin, R. Reininger, T.K. Sham, VLS-PGM beamline at the Canadian light source, AIP Conf. Proc. 879 (2006) 535–538, https://doi.org/10.1063/1.2436116.
[48] G. Donato, D. Holzscherer, J.C. Beam, A.P. Grosvenor, A One-step synthesis of rare-earth phosphate-borosilicate glass composites, RSC Adv. 8 (2018) 39053–39065, https://doi.org/10.1039/C8RA08657E.
[49] A.A. Ahmed, H.A. El-Batal, N.A. Ghoneim, F.A. Khalifa, Leaching of some lithium silicate glasses and glass-ceramics by HCl, J. Non Cryst. Solids 41 (1980) 57–70, https://doi.org/10.1016/0022-3093(80)90191-X.
[50] B.C. Bunker, Molecular mechanisms for corrosion of silica and silicate glasses, J. Non-Cryst. Solids 179 (1994) 300–308, https://doi.org/10.1016/0022-3093(94)90708-0.
[51] M. Fournier, A. Ull, E. Nicoleau, Y. Inagaki, M. Odorico, P. Frugier, S. Gin, Glass dissolution rate measurement and calculation revisited, J. Nucl. Mater. 476 (2016) 140–154, https://doi.org/10.1016/j.jnucmat.2016.04.028.
[52] G. Wen, K. Zhang, D. Yin, H. Zhang, Solid-state reaction synthesis and aqueous durability of Ce-doped zirconolite-rich ceramics, J. Nucl. Mater. 466 (2015) 113–119, https://doi.org/10.1016/j.jnucmat.2015.07.047.
[53] H. Zhu, F. Wang, Q. Liao, Y. Zhu, Synthesis and characterization of zirconolite-sodium borosilicate glass-ceramics for nuclear waste immobilization, J. Nucl. Mater. 532 (2020) 1–10, https://doi.org/10.1016/j.jnucmat.2020.152026.
[54] L.R. Blackburn, R. Crawford, S.A. Walling, L.J. Gardner, M.R. Cole, S. Sun, C. Gausse, A.R. Mason, M.C. Stennett, E.R. Maddrell, N.C. Hyatt, C.L. Corkhill, Influence of accessory phases and surrogate type on accelerated leaching of zirconolite wasteforms, npj Mater. Degrad. 5 (1) (2021) 11, https://doi.org/10.1038/s41529-021-00171-8.
[55] E. Paknahad, A.P. Grosvenor, Investigation of $CeT_{i2}O_6$-and $CaZrTi_2O_7$-containing glass-ceramic composite materials, Can. J. Chem. 95 (2017) 1110–1121, https://doi.org/10.1139/cjc-2016-0633.
[56] H. Aréna, D. Rébiscoul, E. Garcès, N. Godon, Comparative effect of alkaline elements and calcium on alteration of international simple glass, npj Mater. Degrad. 3 (1) (2019) 11, https://doi.org/10.1038/s41529-019-0072-7.
[57] N. Zhang, A. Hedayat, L. Figueroa, K.X. Steirer, H. Li, H.G.B. Sosa, R.P.H. Bernal, N. Tupa, I.Y. Morales, R.S.C. Loza, Experimental studies on the durability and leaching properties of alkali-activated tailings subjected to different environmental conditions, Cem. Concr. Compos. 130 (2022) 1–18, https://doi.org/10.1016/j.cemconcomp.2022.104531.
[58] M.W. Gaultois, A.P. Grosvenor, XANES and XPS investigations of the local structure and final-state effects in amorphous metal silicates: $(ZrO_2)_x(TiO_2)_y(SiO_2)_{1-x-y}$, Phys. Chem. Chem. Phys. 14 (2012) 205–217, https://doi.org/10.1039/C1CP22717C.
[59] B. Gilbert, B.H. Frazer, F. Naab, J.W. Valley, J. Fournelle, G. de Stasio, X-ray absorption spectroscopy of silicates for in situ, sub-micrometer mineral identification, Am. Mineral. 88 (2003) 763–769, https://doi.org/10.2138/am-2003-5-605.
[60] X.L. Wu, S.J. Xiong, J. Zhu, J. Wang, J.C. Shen, P.K. Chu, Identification of surface structures on 3C-SiC nanocrystals with hydrogen and hydroxyl bonding by photoluminescence, Nano Lett. 9 (2009) 4053–4060, https://doi.org/10.1021/nl902226u.
[61] V.A. Terekhov, E.V. Parinova, E.P. Domashevskaya, A.S. Sadchikov, E.I. Terukov, Yu.K. Undalov, B.V. Sen'kovskii, S.Yu Turishchev, Peculiarities of the electronic structure and phase composition of amorphous $(SiO_2)_x$ (a-Si: $H)_{x-1}$ composite films according to X-ray spectroscopy data, Tech. Phys. Lett. 41 (2015) 1010–1012, https://doi.org/10.1134/S1063785015100296.
[62] D.M. Strachan, J.J. Neeway, Effects of alteration product precipitation on glass dissolution, Appl. Geochem. 45 (2014) 144–157, https://doi.org/10.1016/j.apgeochem.2014.03.013.

[63] P. Dillmann, S. Gin, D. Neff, L. Gentaz, D. Rebiscoul, Effect of natural and synthetic iron corrosion products on silicate glass alteration processes, Geochim. Cosmochim. Acta 172 (2016) 287–305, https://doi.org/10.1016/j.gca.2015.09.033.
[64] A.J. Fisher, M.N.B. Imran, C. Mann, C. Gausse, R.J. Hand, N.C. Hyatt, C.L. Corkhill, Short communication: the dissolution of UK simulant vitrified high-level-waste in groundwater solutions, J. Nucl. Mater. 538 (2020) 1–7, https://doi.org/10.1016/j.jnucmat.2020.152245.
[65] A.J. Fisher, M.T. Harrison, N.C. Hyatt1, R.J. Hand, C.L. Corkhill, The dissolution of simulant UK Ca/Zn-modified nuclear waste glass: insight into Stage III behavior, MRS Adv. 5 (2020) 103–109, https://doi.org/10.1557/adv.2020.50.
[66] S. Gin, X. Beaudoux, F. Angéli, C. Jégou, N. Godon, Effect of composition on the short-term and long-term dissolution rates of ten borosilicate glasses of increasing complexity from 3 to 30 oxides, J. Non-Cryst. Solids 358 (2012) 2559–2570, https://doi.org/10.1016/j.jnoncrysol.2012.05.024.
[67] R.D. Shannon, Revised effective ionic radii and systematic studies of interatomic distances in halides and chalcogenides, Acta Cryst. A. 32 (1976) 751–767, https://doi.org/10.1107/S0567739476001551.
[68] M.R. Rafiuddin, G. Donato, S. McCaugherty, A. Mesbah, A.P. Grosvenor, Review of rare-earth phosphate materials for nuclear waste sequestration applications, ACS Omega 7 (2022) 39482–39490, https://doi.org/10.1021/acsomega.2c03271.
[69] G. Topateş, B. Tarhan, M. Tarhan, Chemical durability of zircon containing glass-ceramic glazes, Ceram. Int. 43 (2017) 12333–12337, https://doi.org/10.1016/j.ceramint.2017.06.097.
[70] J.V. Crum, J.J. Neeway, B.J. Riley, Z. Zhu, M.J. Olszta, M. Tang, Dilute condition corrosion behavior of glass-ceramic waste form, J. Nucl. Mater. 482 (2016) 1–11, https://doi.org/10.1016/j.jnucmat.2016.08.002.